Radiative Problems in Black Hole Spacetimes

by

Robert Lee Marsa, B.S.

Dissertation

Presented to the Faculty of the Graduate School of

The University of Texas at Austin

in Partial Fulfillment

of the Requirements

for the Degree of

Doctor of Philosophy

The University of Texas at Austin

December 1995

Radiative Problems in Black Hole Spacetimes

Approved by
Dissertation Comittee:

_____

_____

_____

_____

_____

To Anissa

Acknowledgements

I would like to thank my supervisor, Dr. Matthew Choptuik for his invaluable assistance throughout my graduate studies. In particular, I would like to thank him for directing me to study these problems, for help and advice in solving them, for checks of the equations, and for entertaining and useful discussions.

Special thanks also to Dr. Richard Matzner for his advice, assistance, and hospitality. Thanks to my parents for all their support, and to my wife for *everything.* And thanks to many of my graduate, undergraduate, and high-school teachers who inspired me.

This work was supported in part by the Texas Advanced Research Project TARP-085 to Richard Matzner, the Cray Research Grant to Richard Matzner, and NSF PHY9318152 (ARPA supplemented) to the Grand Challenge Alliance.

Radiative Problems in Black Hole Spacetimes

Publication No. _____

Robert Lee Marsa, Ph.D.
The University of Texas at Austin, 1995

Supervisor: Matthew W. Choptuik

This dissertation investigates finite difference techniques which are useful for solving radiative problems in spacetimes which contain a black hole. The singularities present in such spacetimes are avoided by excising the interior of the black hole from the computational domain. The boundary of the black hole is chosen at the apparent horizon. Spatial derivatives at this boundary are tipped so that they only reference points outside the black hole. Programs using this method are used to examine the interaction of a scalar field with a Schwarzschild black hole in spherical symmetry and with a Kerr black hole in three dimensions.

The main spherically symmetric calculation looks at the scattering of ingoing packets of massless scalar field. *Quasi-normal* ringing and power-law tails are observed, along with interesting coordinate and nonlinear effects. Also examined is the stability of a static solution found by Bechmann and Lechtenfeld. This solution describes a static configuration of scalar field with potential outside a black hole.

The three dimensional calculation looks at the scattering of packets of massless scalar field from a fixed Kerr background. The phenomenon of *superradiance* is examined.

The programs used in this work were constructed using the new prototyping language RNPL. This language allows for the fairly simple construction and modification of programs to solve time-dependent partial differential equations. RNPL and its compiler are discussed near the end of this dissertation.

Contents

List of Figures

List of Tables

Chapter 1. Introduction

As the title suggests, this dissertation is concerned with solving problems involving radiation in spacetimes which contain a black hole. Due to the number and complexity of the equations of general relativity (Einstein's equations), exact solutions are hard to come by except in the simplest situations. Thus, relativists turn to computers and numerical methods to solve more realistic problems. However, computers have difficulty solving these problems as well.

Again, because of the complexity of the equations, and in particular, because of their nonlinear behavior, the Einstein equations are difficult to code in an error free and stable manner. Further, calculations involving strong fields are likely to develop black holes—and with black holes come singularities. It is important to note that these singularities are *physical* singularities near which the curvature scalar quantities experience unbounded growth. As such, they can not be removed by coordinate transformations or other methods typically used to deal with singular points in differential equations.

1.1. Black Holes, Singularities, and Horizon Boundaries

As can be expected, computers, with their finite precision, have great difficulty treating singularities. Thus, the only hope of numerically solving relativistic problems involving generic strong fields or initial black holes is to find some way to "avoid" the singularities which are either present initially or likely to develop.

A common method of avoiding singularities in gravitational collapse is to make use of the coordinate freedom allowed by general relativity to let time elapse at different rates in different parts of the spacetime. In particular, a coordinate system can be chosen so that time slows rapidly as one nears the singularity, stopping before it is reached. This prevents the region of spacetime covered by the chosen coordinate system from ever encountering the

singularity. Unfortunately, this method introduces its own problems. In order to remain at rest (at a fixed coordinate location) near the singularity, an observer will have to experience an unbounded acceleration as proper time progresses. This acceleration term appears in the Einstein equations and will cause the numerical evolution to eventually halt. The space-like physical singularity has been avoided by introducing a time-like coordinate singularity caused by unbounded growth in the field variables. What is needed is a way to avoid the physical singularity without introducing any coordinate singularities.

By definition, black-hole-spacetimes contain event horizons. In fact, the *Cosmic Censorship Conjecture* states that any singularity will always be hidden within such a horizon. Although it is possible to construct certain collapse situations which result in the formation of a "naked" singularity, that is, one not hidden inside a horizon, such situations are unlikely to develop during a generic calculation. Thus we can reasonably expect any singularity that forms during a calculation will be hidden inside an event horizon. This horizon is a closed surface out of which no information can pass. This gives rise to the idea of avoiding singularities by black hole excision. We simply confine our numerical evolution to only those events outside the horizon, ignoring the region of spacetime inside the horizon altogether.

Unfortunately, this method is not without its problems either. Location of the event horizon requires knowledge of the entire spacetime—knowledge not available until the calculation is complete. But apparent horizons can be found from information about the curvature of a single space-like slice. Like an event horizon, an apparent horizon is a trapped surface—a surface through which no light can escape. Further, apparent horizons always lie within the event horizon. Thus, if we stop our numerical domain at the apparent horizon, we may evolve part of the interior of the black hole, but will still avoid any singularities that lie within. Seidel and Suen have used such a scheme with encouraging results (see [22] and [1]).

For the research in this dissertation, I use the same approach, though without the *causal differencing* used in the previous works. I look at the interactions of a massless scalar field with an existing black hole in one and three spatial dimensions. In the 1D case, I evolve the geometric variables along with the scalar field using the full Einstein-Klein-Gordon equations, while in the 3D case, I evolve the scalar field on a *fixed* Kerr background.

1.2. Computer Aided Programming

Even with a good coordinate system and an apparent horizon boundary, solving the Einstein equations is still no simple task. Finding a stable differencing scheme—especially at the boundaries—is a time consuming, iterative task. When a given implementation is unstable, it is often difficult to determine if the problem is due to a coding error or the differencing scheme. Every time the differencing scheme is changed, there is a new opportunity for introducing errors. What is needed is a computer program to assist the numerical physicist. This program should allow difference schemes to be easily changed without introducing errors. It should also assist in other ways by providing robust facilities for check-pointing and output and parameter control.

I have constructed such a system which I call RNPL—Rapid Numerical Prototyping Language. The system includes both the language and a compiler which takes RNPL programs and converts them to C or FORTRAN which can then be compiled and executed on a variety of machines. I used RNPL to write all the programs used in this research.

1.3. Notation and Conventions

Like most numerical relativists, I will be using a metric with signature (–, +, +, +) so that the 3-metric is positive definite. Latin indices ($i, j, k, \ldots$) on tensors range over $\{1, 2, 3\}$ while Greek indices ($\alpha, \beta, \gamma, \ldots$) range over $\{0, 1, 2, 3\}$. I observe the Einstein summation convention in which repeated indices indicate a sum over the repeated index. ∇_α represents covariant differentiation with respect to the four-metric, D_α represents covariant differentiation with respect to the three-metric, and ∂_α represents ordinary partial differentiation. I adopt geometricized units in which $G = c = 1$.

As is usual when discussing numerical analysis, discretized functions use superscripts for the time index and subscripts for the spatial indices. For instance, $f^n_{i,j,k} \equiv f(n\Delta t, i\Delta x^1, j\Delta x^2, k\Delta x^3)$. Further, in discussions of finite difference equations, n will refer to the time level, while $i, j,$ and k will refer to the spatial grid location.

Chapter 2. Equations and Methods

2.1. General 3 + 1 Equations

The derivation of the 3 + 1 form of the Einstein equations has been carried out in detail many times (see for example [24] and [18]). Here, I will simply give a brief description of the 3 + 1 method and state the equations in a coordinate independent form as given in [13]. However, I will show the derivation of the Klein-Gordon equation.

In order to write the equations in 3 + 1 form, we must break the coordinates into one "time" coordinate and three "space" coordinates. To do this, we choose a "time" function t and use it to "slice" spacetime into a set of hypersurfaces Σ_t of constant t. We also choose a "time flow" vector field t^μ satisfying $t^\mu \nabla_\mu t = 1$. If n^μ is a unit vector field normal to the Σ_t, we can decompose t^μ into parts normal and tangential to Σ_t.

$$t^\mu = \alpha n^\mu + \beta^\mu. \tag{2.1.1}$$

Equation (2.1.1) defines the *lapse* function α and the *shift* vector β^i. Given the normal n^μ, we can define the three-metric by:

$$h_{\mu\nu} = g_{\mu\nu} + n_\mu n_\nu. \tag{2.1.2}$$

The *extrinsic curvature* is defined as:

$$K_{ij} \equiv \frac{1}{2} \pounds_n h_{ij}, \tag{2.1.3}$$

where $\pounds_n$ is the Lie derivative along n^μ. Written in 3 + 1 form, the line element is:

$$ds^2 = -\alpha^2 dt^2 + h_{ij}\left(dx^i + \beta^i dt\right)\left(dx^j + \beta^j dt\right). \tag{2.1.4}$$

The metric and its inverse in matrix notation are:

$$g_{\mu\nu} = \begin{pmatrix} -\alpha^2 + \beta^i\beta_i & \beta_j \\ \beta_i & h_{ij} \end{pmatrix}, \tag{2.1.5}$$

and

$$g^{\mu\nu} = \begin{pmatrix} -\frac{1}{\alpha^2} & \frac{\beta^i}{\alpha^2} \\ \frac{\beta^j}{\alpha^2} & h^{ij} - \frac{\beta^i\beta^j}{\alpha^2} \end{pmatrix}. \tag{2.1.6}$$

The covariant form of the Klein-Gordon equation is

$$\nabla^\mu \nabla_\mu \phi = \partial_\phi V(\phi), \tag{2.1.7}$$

where $V(\phi)$ is an interaction potential. This reduces to

$$\frac{1}{\sqrt{-g}}\,\partial_\mu\left(\sqrt{-g}\,g^{\mu\nu}\partial_\nu\phi\right) = \partial_\phi V(\phi), \tag{2.1.8}$$

where g is the determinant of the metric. If we multiply by $\sqrt{-g}$ then the right hand side is simply $\alpha\sqrt{h}\,\partial_\phi V$, where h is the determinant of the three-metric. From the left hand side, we get

$$\partial_t\left(\alpha\sqrt{h}\,g^{t\nu}\partial_\nu\phi\right) + \partial_i\left(\alpha\sqrt{h}\,g^{i\nu}\partial_\nu\phi\right) =$$

$$\partial_t\left[\alpha\sqrt{h}\left(g^{tt}\partial_t\phi + g^{ti}\partial_i\phi\right)\right] + \partial_i\left[\alpha\sqrt{h}\left(g^{it}\partial_t\phi + g^{ij}\partial_j\phi\right)\right] =$$

$$\partial_t\left[\frac{\sqrt{h}}{\alpha}\left(\beta^i\partial_i - \partial_t\right)\phi\right] + \partial_i\left[\frac{\sqrt{h}}{\alpha}\,\beta^i\left(\partial_t - \beta^j\right)\phi + \alpha\sqrt{h}\,h^{ij}\partial_j\phi\right] =$$

$$\partial_t\left[\frac{\sqrt{h}}{\alpha}\left(\beta^i\partial_i - \partial_t\right)\phi\right] - \partial_i\beta^i\left[\frac{\sqrt{h}}{\alpha}\left(\beta^j - \partial_t\right)\phi\right] + \partial_i\left(\alpha\sqrt{h}\,h^{ij}\partial_j\phi\right) = \alpha\sqrt{h}\,\partial_\phi V\,. \tag{2.1.9}$$

If we define four auxiliary variables by

$$\Pi \equiv \frac{\sqrt{h}}{\alpha}\left(\partial_t - \beta^i \partial_i\right)\phi\,, \tag{2.1.10}$$

and

$$\Phi_i \equiv \partial_i \phi\,, \tag{2.1.11}$$

then we can write (2.1.9) as an evolution equation for Π, namely

$$\partial_t \Pi = \partial_i\Big(\beta^i \Pi + \alpha\sqrt{h}\left(h^{ij}\Phi_j\right)\Big) - \alpha\sqrt{h}\,\partial_\phi V. \tag{2.1.12}$$

Differentiating (2.1.10) gives us evolution equations for the three Φ variables

$$\partial_t \Phi_i = \partial_i\Big(\frac{\alpha}{\sqrt{h}}\,\Pi + \beta^j \Phi_j\Big). \tag{2.1.13}$$

The Einstein equations in 3 + 1 form are

$$R + K^2 - K_{ij}K^{ij} = 16\pi\rho_H\,, \tag{2.1.14}$$

$$D_i K^i{}_j - D_j K = 8\pi S_j\,, \tag{2.1.15}$$

$$\partial_t K^i{}_j = -D^i D_j \alpha + \alpha\Big[R^i{}_j + K K^i{}_j - 8\pi S^i{}_j + 4\pi\delta^i{}_j\left(S - \rho_H\right)\Big], \tag{2.1.16}$$

$$\partial_t h_{ij} = -2\,\alpha K_{ij} + D_i\beta_j + D_j\beta_i\,, \tag{2.1.17}$$

where $R^i{}_j$ is the Ricci tensor and R is the Ricci scalar. The source terms for the scalar field are

$$\rho_H = \frac{1}{2}h^{ij}\Phi_i\Phi_j + \frac{1}{2h}\,\Pi^2 + V\left(\phi\right) \tag{2.1.18}$$

$$S^i = -\frac{\Pi}{\sqrt{h}}\,h^{ij}\Phi_j \tag{2.1.19}$$

$$S^{ij} = h^{ij}\Big(-\frac{1}{2}h^{kl}\Phi_k\Phi_l + \frac{1}{2h}\Pi^2 - V(\phi)\Big) + h^{ik}h^{jl}\Phi_k\Phi_l \tag{2.1.20}$$

$$S = -\frac{1}{2}h^{ij}\Phi_i\Phi_j + \frac{3}{2h}\Pi^2 - 3V(\phi). \tag{2.1.21}$$

Substituting the source terms into equation (2.1.16), we get

$$\frac{1}{\alpha}(\partial_t - \beta^k\partial_k)K^i_{\ j} = KK^i_{\ j} - \frac{1}{\alpha}h^{ik}\left(\partial_j\partial_k\alpha - \Gamma^l_{\ jk}\partial_l\alpha\right) + R^i_{\ j}$$

$$-8\pi\Big(h^{ik}\Phi_k\Phi_j + \delta^i_{\ j}V(\phi)\Big) + \frac{1}{\alpha}\left(K^i_{\ k}\partial_j\beta^k - K^k_{\ j}\partial_k\beta^i\right). \tag{2.1.22}$$

Similarly, equation (2.1.17) becomes

$$\frac{1}{\alpha}(\partial_t - \beta^k\partial_k)h_{ij} = -2K_{ij} + \frac{1}{\alpha}\left(h_{ki}\partial_j\beta^k + h_{kj}\partial_i\beta^k\right). \tag{2.1.23}$$

The Hamiltonian constraint (2.1.14) becomes

$$R + K^2 - K_{ij}K^{ij} = 16\pi\Big(\frac{1}{2}h^{ij}\Phi_i\Phi_j + \frac{1}{2h}\Pi^2 + V(\phi)\Big) \tag{2.1.24}$$

and the momentum constraints (2.1.15) become

$$D_iK^i_{\ j} - D_jK = -8\pi\frac{\Pi}{\sqrt{h}}\Phi_j. \tag{2.1.25}$$

2.2. Numerical Analysis

There are many problems that can occur when trying to solve a set of partial differential equations numerically. As mentioned in Section 1.2, when an attempted solution method proves unstable, it is often difficult to determine the cause of the problem. Is it a programming error or is it the finite difference scheme?

More importantly, if the solution method appears to be stable, we need rigorous methods for deciding if it really is stable, and if so, is it in fact solving the correct set of equations.

Following [6] and [8], I will give some methods for rigorously determining the correctness and stability of a finite difference scheme.

2.2.1. Definitions

We are concerned with numerically solving a set of continuum partial differential equations using finite differencing. This means that we apply finite difference approximations of the differential operators to discretized versions of the functions. I will represent the discretized versions of functions and operators by hatted quantities, while using unhatted quantities for the continuum versions.

Given a function u and a differential operator L satisfying the equation

$$Lu = 0, \tag{2.2.1.1}$$

we define the *truncation error* by

$$\hat{\tau} \equiv \hat{L}u \tag{2.2.1.2}$$

and the solution error by

$$\hat{e} \equiv u - \hat{u}. \tag{2.2.1.3}$$

We say that the finite difference operator is pth-order accurate if $\hat{\tau} = O\left(h^p\right)$, when acting on a function discretized on a grid with spacing h. The schemes I will be using in this dissertation are all 2nd-order accurate, so for the remaining discussion I will assume $p = 2$.

If $\hat{L}$ is made up of centered difference operators, then as the grid spacing goes to zero, we get the following continuum expansion for the discretized function [21]:

$$\hat{u} = u - h^2 e_2 - h^4 e_4 - \cdots, \tag{2.2.1.4}$$

where e_i is an h-independent error function. Similarly, if $\hat{L}$ is not completely centered, we will, in general, get the following continuum expansion for the discretized function:

$$\hat{u} = u - h^2 e_2 - h^3 e_3 - h^4 e_4 - \cdots. \tag{2.2.1.5}$$

2.2.2. Methods

Assume that we have a program to generate solutions to the system $\hat{L}\hat{u} = 0$. This program appears to be stable, that is, for the time we have evolved the solution, nothing has "blown up." How can we check to make sure the method is really stable? We must check for convergence. If the solution is not convergent, then it is not stable.

To check for convergence, we must compute solutions on three grids with different resolutions. It is convenient to choose one with spacing h, one with spacing $2h$, and one with spacing $4h$. We will call these solutions $\hat{u}_h$, $\hat{u}_{2h}$, and $\hat{u}_{4h}$, respectively. From (2.2.1.4), we can see that for a centered scheme, these solutions should have the following expansions:

$$\hat{u}_h = u - h^2 e_2 - h^4 e_4 - \cdots$$

$$\hat{u}_{2h} = u - 4h^2 e_2 - 16h^4 e_4 - \cdots$$

$$\hat{u}_{4h} = u - 16h^2 e_2 - 256h^4 e_4 - \cdots.$$

Then

$$\hat{u}_{2h} - \hat{u}_{4h} = 12h^2 e_2 + 240h^4 e_4 + \cdots$$

and

$$\hat{u}_h - \hat{u}_{2h} = 3h^2 e_2 + 15h^4 e_4 + \cdots.$$

The *convergence factor* is defined as

$$C_f \equiv \frac{\hat{u}_{2h} - \hat{u}_{4h}}{\hat{u}_h - \hat{u}_{2h}}. \tag{2.2.2.1}$$

In this case, $C_f = 4 + O(h^2)$. Going through a similar series of expansions, we can see that for a 1st-order accurate scheme we get $C_f = 2 + O(h^2)$. If the difference operators are not properly centered, then we will get $C_f = 4 + O(h)$ and $C_f = 2 + O(h)$ for 2nd and 1st-order schemes.

Thus, if we've constructed a 2nd-order accurate scheme, we should expect the convergence factor to be approximately four. If we compute a convergence factor that is less than one, we know that the scheme is unstable. If we make the grid spacing small enough, the solution will "blow up." However, if we compute a convergence factor of four, then we know the scheme is stable for the data being evolved. Other data can cause the scheme to exhibit other behavior, especially if the equations are nonlinear. It is important to check any interesting or unexpected solutions for convergence to make sure they are not numerical artifacts.

The fact that a program is stable and convergent simply means that it is correctly solving the set of algebraic finite-difference equations. In order to show that it is actually approximating the desired set of differential equations, we construct another finite difference approximation to L which we will call $\tilde{L}$. We then compute $\tilde{L}\hat{u}$. For a 2nd-order, centered approximation, we should get

$$\tilde{L}\hat{u} = h^2 f_2 + h^4 f_4 + \cdots,$$

where again, f_2, f_4, etc. are h-independent error functions. We then compute the convergence factor from $\left(\tilde{L}\hat{u}_h,\ \tilde{L}\hat{u}_{2h},\ \tilde{L}\hat{u}_{4h}\right)$. If we get four, then we can be sure that we are solving the desired set of equations. $\tilde{L}\hat{u}$ is called a *residual* and since $\hat{u}$ was found using $\hat{L}$, $\tilde{L}$ is called an *independent* residual evaluator.

Chapter 3. Spherical Symmetry I: Theory

3.1. Spherically Symmetric Einstein-Klein-Gordon Equations

The Einstein-Klein-Gordon equations (see Section 2.1) can be specialized to spherical symmetry resulting in a tremendous simplification of the system. I will adopt the usual names for spherical coordinates, namely $\left(t, r, \theta, \phi\right)$. In this coordinate system, h_{ij} and $K^{i}_{\ j}$ are diagonal. We have

$$h_{ij} = \mathrm{diag}\left(a^2\left(t,r\right), r^2 b^2\left(t,r\right), r^2 b^2 \sin^2\theta\right) \tag{3.1.1}$$

$$K^{i}_{\ j} = \mathrm{diag}\left(K^{r}_{\ r}\left(t,r\right), K^{\theta}_{\ \theta}\left(t,r\right), K^{\theta}_{\ \theta}\right) \tag{3.1.2}$$

$$\beta^{i} = \left(\beta^{r}\left(t,r\right), 0, 0\right) \equiv \left(\beta, 0, 0\right) \tag{3.1.3}$$

$$\alpha = \alpha\left(t,r\right), \phi = \phi\left(t,r\right). \tag{3.1.4}$$

$$\Phi_{i} = \left(\Phi_{r}\left(t,r\right), 0, 0\right) \equiv \left(\Phi, 0, 0\right) \tag{3.1.5}$$

The Christoffel symbols are given by

$$\Gamma^{i}_{\ jk} = \frac{1}{2} h^{il}\left(\partial_k h_{lj} + \partial_j h_{lk} - \partial_i h_{jk}\right). \tag{3.1.6}$$

In spherical symmetry, the non-zero components are

$$\Gamma^{r}_{\ rr} = \frac{\partial_r a}{a} \qquad \Gamma^{r}_{\ \theta\theta} = -\frac{rb\partial_r\left(rb\right)}{a^2} \qquad \Gamma^{\theta}_{\ r\theta} = \frac{\partial_r\left(rb\right)}{rb}$$

$$\Gamma^{r}{}_{\phi\phi} = -\sin^2\theta\,\frac{rb\partial_r(rb)}{a^2} \qquad \Gamma^{\phi}{}_{r\phi} = \frac{\partial_r(rb)}{rb}$$
$$\Gamma^{\theta}{}_{\phi\phi} = -\sin\theta\cos\theta \qquad \Gamma^{\phi}{}_{\phi\theta} = -\cot\theta$$

The two non-zero components of the Ricci tensor are

$$R^{r}{}_{r} = -\frac{2}{arb}\,\partial_r\,\frac{\partial_r(rb)}{a} \tag{3.1.7}$$

$$R^{\theta}{}_{\theta} = \frac{1}{ar^2b^2}\left[a - \partial_r\left(\frac{rb}{a}\,\partial_r(rb)\right)\right]. \tag{3.1.8}$$

From now on, we will denote ∂_r by a prime and ∂_t by an over dot. Equation (2.1.23) becomes

$$\dot{a} = -a\alpha K^{r}{}_{r} + (a\beta)' \tag{3.1.9}$$

$$\dot{b} = -\alpha b K^{\theta}{}_{\theta} + \frac{\beta}{r}(r\beta)'. \tag{3.1.10}$$

For the extrinsic curvature (2.1.22) we get

$$\dot{K^{r}{}_{r}} = \beta K^{r}{}_{r}{}' + \alpha K^{r}{}_{r} K - \frac{1}{a}\left(\frac{\alpha'}{a}\right)' - \frac{2\alpha}{arb}\left[\frac{(rb)'}{a}\right]' - \pi\alpha\left(\frac{\Phi^2}{a^2} + V(\phi)\right) \tag{3.1.11}$$

$$\dot{K^{\theta}{}_{\theta}} = \beta K^{\theta}{}_{\theta}{}' + \alpha K^{\theta}{}_{\theta} K + \frac{\alpha}{(rb)^2} - \frac{1}{a(rb)^2}\left(\frac{\alpha rb}{a}(rb)'\right)' - 8\pi V(\phi). \tag{3.1.12}$$

Following [6] we change our definition for Π slightly

$$\Pi \to \frac{1}{r^2b^2\sin\theta}\,\Pi = \frac{a}{\alpha}\left(\dot{\phi} - \beta\phi'\right), \tag{3.1.13}$$

while the definition for Φ remains the same

$$\Phi \equiv \phi'. \tag{3.1.14}$$

Using these variables, (2.1.12) becomes

$$\dot{\Pi} = \frac{1}{r^2 b^2}\Big[r^2 b^2\left(\beta\Pi + \frac{\alpha}{a}\Phi\right)\Big]' - 2\Pi\,\frac{\dot{b}}{b} - \alpha a \partial_\phi V \tag{3.1.15}$$

and (2.1.13) becomes

$$\dot{\Phi} = \left(\beta\Phi + \frac{\alpha}{a}\Pi\right)'. \tag{3.1.16}$$

The Hamiltonian constraint (2.1.24) is

$$-\frac{2}{arb}\left[\left(\frac{(rb)'}{a}\right)' + \frac{1}{rb}\left(\left(\frac{rb}{a}(rb)'\right)' - a\right)\right] + 4K^r{}_r\,K^\theta{}_\theta + 2K^\theta{}_\theta{}^2 =$$

$$8\pi\left(\frac{\Phi^2 + \Pi^2}{a^2} + 2V(\phi)\right) \tag{3.1.17}$$

and the momentum constraint (2.1.25) is

$$\frac{(rb)'}{rb}\left(K^\theta{}_\theta - K^r{}_r\right) - K^\theta{}_\theta{}' = -4\pi\,\frac{\Phi\Pi}{a}\,. \tag{3.1.18}$$

3.2. Minimally-Modified Ingoing Eddington-Finkelstein Coordinates

For the spherically symmetric calculations, I use a coordinate system introduced in [7] from earlier work [5]. Figure 3.1 shows how the Ingoing Eddington-Finkelstein coordinates relate to Kruskal-Szekeres coordinates. Notice that the slices all penetrate the horizon and meet the singularity.

To specify this coordinate system mathematically, we must fix the lapse and the shift. First, we introduce a "shifted" areal coordinate s defined by $s \equiv r + f\left(t\right)$ for some as yet undetermined function f. Our metric is now

$$ds^2 = \left(-\alpha^2 + a^2\beta^2\right)dt^2 + 2a^2\beta\,dtdr + a^2dr^2 + s^2d\Omega^2. \tag{3.2.1}$$

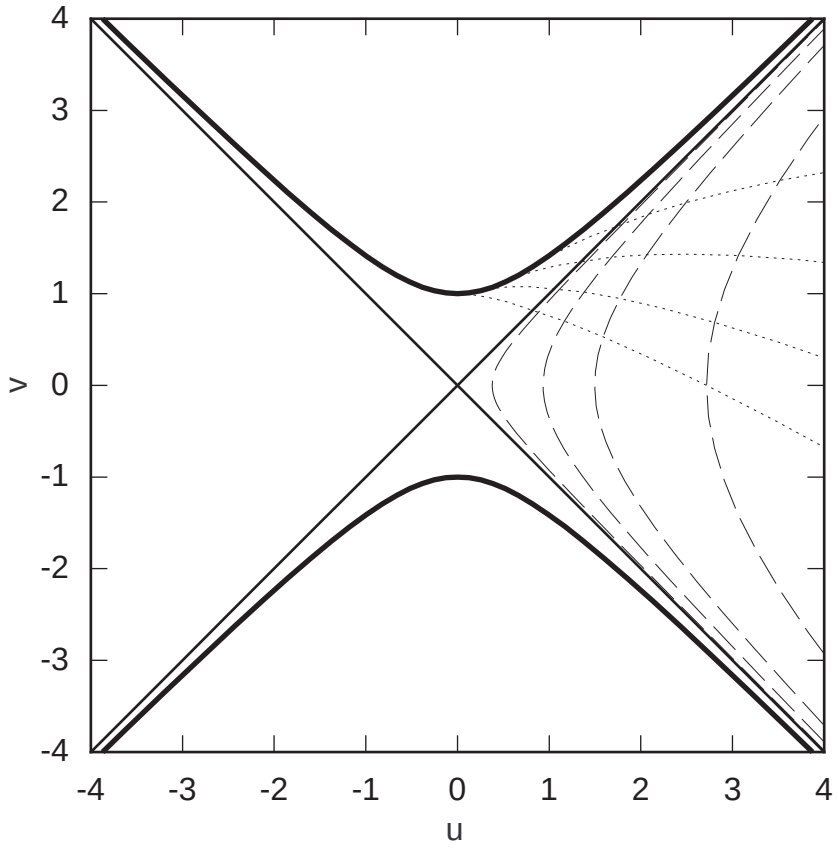

Figure 3.1. The Ingoing Eddington-Finkelstein slices in Kruskal-Szekeres coordinates. The dotted lines are constant t, while the dashed lines are constant r. The dark curves are the singularity. The diagonal lines are the horizon ($r = 2M$).

From this we see that $s = rb$ so $b = 1 + \frac{f}{r}$. Then from (3.1.10) we see that

$$\left(\dot{rb}\right) = -\alpha rbK^{\theta}{}_{\theta} + \beta\left(rb\right)' \tag{3.2.2}$$

and hence

$$\beta = \dot{f} + s\alpha K^{\theta}{}_{\theta}\,. \tag{3.2.3}$$

To set the lapse, we demand that the ingoing combination of tangent vectors $\vec{\partial}_t - \vec{\partial}_r$ be null. This gives a condition on the metric, namely $g_{tt} - 2g_{tr} + g_{rr} = 0$. Using (3.2.1) this implies

$$\alpha = \pm a\left(1-\beta\right). \tag{3.2.4}$$

We choose the sign so α is positive for $\left|\beta\right| \leq 1$, that is $\alpha = a\left(1-\beta\right)$. Using (3.2.3) and (3.2.4) we get

$$\beta = \frac{\dot{f} + saK^{\theta}{}_{\theta}}{1 + saK^{\theta}{}_{\theta}} \tag{3.2.5}$$

$$\alpha = \frac{a\left(-\dot{f}\right)}{1 + saK^{\theta}{}_{\theta}}. \tag{3.2.6}$$

And hence, the metric takes the form

$$ds^2 = a^2\left(2\beta - 1\right)dt^2 + 2a^2\beta\, dtdr + a^2dr^2 + s^2d\Omega^2. \tag{3.2.7}$$

Factoring the first three terms yields

$$ds^2 = a^2\Big(\left(2\beta - 1\right)dt + dr\Big)\left(dt + dr\right) + s^2d\Omega^2, \tag{3.2.8}$$

which shows that the characteristic speeds are

$$c = -1,\ 1-2\beta\,. \tag{3.2.9}$$

Now we are ready to write down the evolution and constraint equations in their final form. The constraints are

$$a' + \frac{1}{2s}\left(a^3 - a\right) + \frac{a^3s}{2}K^{\theta}{}_{\theta}\left(2K^{r}{}_{r} + K^{\theta}{}_{\theta}\right) - 2\pi sa\Big(\Phi^2 + \Pi^2 + 2a^2V\left(\phi\right)\Big) = 0\,, \tag{3.2.10}$$

$$K^{\theta}{}_{\theta}{}' + \frac{K^{\theta}{}_{\theta} - K^{r}{}_{r}}{s} - \frac{4\pi\Phi\Pi}{a} = 0. \tag{3.2.11}$$

The evolution equations are

$$\dot{a} = -a^2(1-\beta)K^r{}_r + (a\beta)', \tag{3.2.12}$$

$$\dot{K^\theta{}_\theta} = \beta K^\theta{}_\theta{}' + a(1-\beta)\left(K^\theta{}_\theta(K^r{}_r + 2K^\theta{}_\theta) - 8\pi V(\phi)\right) + \frac{1-\beta}{s^2}\left(a - \frac{1}{a}\right) + \frac{\beta'}{as}, \tag{3.2.13}$$

$$\dot{K^r{}_r} = \beta K^r{}_r{}' + a(1-\beta)K^r{}_r(K^r{}_r + 2K^\theta{}_\theta) +$$

$$\frac{\beta-1}{a}\left[\frac{a''}{a} - \left(\frac{a'}{a}\right)^2 - \frac{2a'}{sa} + 8\pi\left(\Phi^2 + a^2 V(\phi)\right)\right] + \frac{\beta' a'}{a^2} + \frac{\beta''}{a}, \tag{3.2.14}$$

$$\dot{\Phi} = \left(\beta\Phi + (1-\beta)\Pi\right)', \tag{3.2.15}$$

$$\dot{\Pi} = \frac{1}{s^2}\left[s^2\left(\beta\Pi + (1-\beta)\Phi\right)\right]' - \frac{2\dot{s}}{s}\Pi - a^2(1-\beta)\partial_\phi V. \tag{3.2.16}$$

We can get an evolution equation for f from the apparent horizon equation. If s^μ is an outward-pointing, space-like unit normal to a trapped surface, then it obeys the equation [6]

$$D_i s^i - K + s^i s^j K_{ij} = 0. \tag{3.2.17}$$

In spherical symmetry, this reduces to

$$(rb)' - arbK^\theta{}_\theta = 0, \tag{3.2.18}$$

which, in MMIEF is simply

$$asK^\theta{}_\theta = 1. \tag{3.2.19}$$

To keep the horizon at fixed r, we demand that $\left(as\dot{K^\theta{}_\theta}\right)\Big|_{r_h} = 0$, where r_h is the initial position of the apparent horizon, $r = 2M$. This gives the following equation for $\dot{f}$:

$$\dot{f} = \left.\frac{4\pi s^2(\Phi+\Pi)^2}{a^2(1-8\pi s^2 V(\phi))}\right|_{r^*}. \tag{3.2.20}$$

Since we wish to examine spacetimes which contain a black hole, it will be useful to write down the Schwarzschild solution in MMIEF coordinates. First, we note that the Ingoing Eddington-Finkelstein metric is usually written as [18]:

$$ds^2 = -\left(1-\frac{2M}{r}\right)d\tilde{V}^2 + 2d\tilde{V}dr + r^2 d\Omega^2. \tag{3.2.21}$$

Instead of using the null coordinate $\tilde{V}$, we can use a time-like coordinate defined as $t \equiv \tilde{V} - r$. With this coordinate, the metric becomes

$$ds^2 = -\left(1-\frac{2M}{r}\right)dt^2 + \frac{4M}{r}\,dtdr + \left(1+\frac{2M}{r}\right)dr^2 + r^2 d\Omega^2. \tag{3.2.22}$$

We can then set this equal to the 3 + 1 metric (3.2.7) to determine the 3 + 1 form of the Schwarzschild solution in these coordinates. The results are:

$$\alpha = \sqrt{\frac{r}{r+2M}}, \tag{3.2.23}$$

$$\beta = \frac{2M}{r+2M}, \tag{3.2.24}$$

$$a = \sqrt{\frac{r+2M}{r}}. \tag{3.2.25}$$

Using these and equations (3.1.9) and (3.1.10), we can find the extrinsic curvature components.

$$K^{\theta}{}_{\theta} = \frac{2M\left(r+2M\right)}{\left(r\left(r+2M\right)\right)^{3/2}}, \tag{3.2.26}$$

$$K^{r}{}_{r} = \frac{-2M\left(r+M\right)}{\left(r\left(r+2M\right)\right)^{3/2}}. \tag{3.2.27}$$

Finally, we note that the mass in these coordinates can be computed from the surface area

as

$$M(s) = \frac{1}{2}s\left(1 - \left(16\pi\mathcal{A}\right)^{-1}\mathcal{A}^{,\mu}\mathcal{A}_{,\mu}\right), \tag{3.2.28}$$

where $\mathcal{A} \equiv 4\pi s^2$. In MMIEF, this becomes

$$M(r) = \frac{1}{2}s\left(1 - \frac{1 - \left(saK^{\theta}{}_{\theta}\right)^2}{a^2}\right). \tag{3.2.29}$$

By making use of the evolution and constraint equations, we can write this mass as an integral over the mass-density. In this form we have

$$M(r) = \frac{s_h}{2} + 4\pi\int_{r_h}^{r} s^2\left(\frac{\Phi^2 + \Pi^2}{2a^2} + sK^{\theta}{}_{\theta}\frac{\Phi\Pi}{a} + V(\phi)\right)dr\,, \tag{3.2.30}$$

where r_h is the location of the apparent horizon and s_h is the value of s at r_h. Both forms of the mass will be computed numerically to provide checks on the accuracy of the program.

3.3. Regularity at the Origin

In cases where a black hole is not initially present or there is insufficient mass in the scalar field to form a black hole through collapse, the infalling matter will encounter the coordinate origin. The origin is one boundary of the computational domain, so we need boundary conditions to find the function values at this point. Since this is not a physical boundary, however, we do not have boundary values. Rather we must use regularity conditions to determine the behavior of the functions near the origin (see [2] for an extensive discussion).

3.3.1. Expansions

Since ϕ is a scalar and $a, K^{\theta}{}_{\theta}$, and $K^{r}{}_{r}$ are elements of rank-two tensors, we know they are even in r. Thus, near the origin, they have the following expansions:

$$\phi(r) = \phi_0 + \phi_2 r^2 + \phi_4 r^4 + \cdots \tag{3.3.1.1}$$

$$a(r) = a_0 + a_2 r^2 + a_4 r^4 + \cdots \tag{3.3.1.2}$$

$$K^{\theta}{}_{\theta}(r) = k_0 + k_2 r^2 + k_4 r^4 + \cdots \tag{3.3.1.3}$$

$$K^{r}{}_{r}(r) = K_0 + K_2 r^2 + K_4 r^4 + \cdots. \tag{3.3.1.4}$$

These expansions immediately give us the following conditions on the spatial derivatives:

$$\phi' = 0 \tag{3.3.1.5}$$

$$a' = 0 \tag{3.3.1.6}$$

$$K^{\theta}{}_{\theta}{}' = 0 \tag{3.3.1.7}$$

$$K^{r}{}_{r}{}' = 0\,. \tag{3.3.1.8}$$

3.3.2. Geometric Variables

Since our spacetime must be locally flat near the origin, we have $a(0) = 1$. An examination of the momentum constraint shows that $K^{\theta}{}_{\theta} = K^{r}{}_{r}$ at the origin. We can find further conditions by examining the potentially divergent terms in (3.2.13). These terms are the ones with powers of r in the denominator. When collected, they can be written as

$$\frac{\left(1-\beta\right)\left(a^2-1\right) + r\beta'}{r^2 a}\,. \tag{3.3.2.1}$$

Clearly, as $r \to 0$ both the numerator and the denominator of (3.3.2.1) go to zero. Thus we must use l'Hôspital's rule to find the correct limit. The derivative of the numerator is $2\left(1-\beta\right)aa' - \beta'\left(a^2-1\right) + \beta' + r\beta''$. As $r \to 0$ this goes to β'. The derivative of the denominator is $r^2 a' + 2ra$. Clearly this goes to zero as r goes to zero. Thus, we must have

$\lim_{r\to 0}\beta' = 0$.

Since we still have zero over zero we use l'Hôspital's rule again. The derivative of the numerator is $(1-\beta)\left(2aa'' + 2(a')^2\right) - \beta''(a^2-1) - 2a\beta' a' + 2\beta'' + r\beta'''$. As r goes to zero, this goes to $2(1-\beta)a'' + 2\beta''$. The derivative of the denominator is $r^2 a'' + 4ra' + 2a$. The limit of this is 2. Thus, the limit as $r \to 0$ of equation (3.3.2.1) is $(1-\beta)a'' + \beta''$.

Let us take a moment to examine the structure of β. When there is no black hole present, the shift is defined by

$$\beta = \frac{raK^{\theta}{}_{\theta}}{1 + raK^{\theta}{}_{\theta}}. \tag{3.3.2.2}$$

From this we can easily see that β is zero at the origin. Now

$$\beta' = \frac{raK^{\theta}{}_{\theta}{}' + ra'K^{\theta}{}_{\theta} + aK^{\theta}{}_{\theta}}{\left(1 + raK^{\theta}{}_{\theta}\right)^2}. \tag{3.3.2.3}$$

So,

$$0 = \lim_{r\to 0}\beta' = K^{\theta}{}_{\theta} \Rightarrow K^{\theta}{}_{\theta}(0) = 0. \tag{3.3.2.4}$$

Now the second derivative of β is

$$\beta'' = \frac{raK^{\theta}{}_{\theta}{}'' + 2aK^{\theta}{}_{\theta}{}' + 2ra'K^{\theta}{}_{\theta}{}' + 2a'K^{\theta}{}_{\theta} + ra''K^{\theta}{}_{\theta}}{\left(1 + raK^{\theta}{}_{\theta}\right)^2} - \frac{2\left((raK^{\theta}{}_{\theta})'\right)^2}{\left(1 + raK^{\theta}{}_{\theta}\right)^3}. \tag{3.3.2.5}$$

As r goes to zero, this expression vanishes. Thus, $\beta''(0) = 0$.

Since $K^{\theta}{}_{\theta}$ is fixed at the origin, we must have the right hand of (3.2.13) side vanish. This will only happen if the limit of (3.3.2.1) is zero. This limit is zero only if $a'' = 0$ at the origin.

3.3.3. Scalar Field

The evolution of the scalar field is accomplished through two auxiliary variables, Φ and Π. These are defined by (3.1.14) and (3.1.13). The condition on Φ is obvious (see (3.3.1.5)), namely

$$\Phi(0) = 0. \tag{3.3.3.1}$$

The condition on Π however, is a bit more complicated. First, since the slicing condition gives $\alpha = a(1-\beta)$, we have $a\alpha^{-1} = (1-\beta)^{-1}$. Further, the shift is given by equation (3.3.2.2). Thus, we have $\Pi(0) = \dot{\phi}(0) \neq 0$. We look, then, to Π'. We have

$$\Pi' = \dot{\phi}' + \left(raK^{\theta}{}_{\theta}\right)'\left(\dot{\phi} - \phi'\right) + raK^{\theta}{}_{\theta}\left(\dot{\phi}' - \phi''\right). \tag{3.3.3.2}$$

As $r \to 0$ we see that $\Pi' \to aK^{\theta}{}_{\theta}\dot{\phi} \to 0$. Thus we have the condition

$$\Pi'(0) = 0. \tag{3.3.3.3}$$

3.3.4. Summary

We have three conditions on a

$$a(0) = 1,$$

$$a'(0) = 0,$$

$$a''(0) = 0.$$

Thus, the expansion for a is $a = 1 + a_4 r^4 + a_6 r^6 + \cdots$.

We have four conditions on the extrinsic curvature

$$K^{\theta}{}_{\theta}(0) = 0,$$

$$K^{\theta}{}_{\theta}{}'(0) = 0,$$

$$K^{r}{}_{r}(0) = 0,$$

$$K^{r}{}_{r}{}'(0) = 0.$$

Thus, the expansions for the extrinsic curvature components are $K^{\theta}{}_{\theta} = k_2 r^2 + k_4 r^4 + \cdots$ and $K^{r}{}_{r} = K_2 r^2 + K_4 r^4 + \cdots$.

And finally, we have three conditions on the scalar field variables

$$\Phi(0) = 0,$$

$$\Pi(0) \neq 0,$$

$$\Pi'(0) = 0.$$

Thus, the expansions are $\Phi = 2\phi_2 r + 4\phi_4 r^3 + \cdots$ and $\Pi = \dot{\phi}_0 + \dot{\phi}_2 r^2 + \cdots$.

Unfortunately, these conditions are inconsistent with the Hamiltonian constraint, equation (3.2.10). The spatial derivative of this equation gives an expression for a''. Upon taking the limit of this expression as $r \to 0$, we see that $a'' \propto \Pi^2 \neq 0$. This leads us to the conclusion that the MMIEF coordinate system will admit no non-singular curvature at the origin. The only consistent solutions near the origin are flat space or a black hole. Thus, MMIEF is only a "good" coordinate system to use when a black hole already exists in the spacetime. In a spacetime without a black hole, the equations will remain consistent as long as no energy encounters the origin. This will be the case if the scalar field is outgoing or if it collapses to form a black hole before it encounters the origin. For a collapse problem, the best thing to do would be to start with another coordinates system and change to MMIEF coordinates if a horizon forms. If no horizon forms, there is really no need for the special horizon tracking properties of MMIEF coordinates anyway.

3.4. Initial Data

In order to perform a calculation, we must have initial data for six functions $\left(\Phi, \Pi, \beta, a, K^{\theta}{}_{\theta}, K^{r}{}_{r}\right)$. These functions must satisfy three equations, (3.2.10), (3.2.11), and (3.2.5). This means that three of these functions can be arbitrarily specified.

I wish to examine the the "scattering" of compact (mostly) ingoing pulses of scalar radiation off a black hole. The word *scattering* is in quotes because scattering doesn't always occur. Long enough wavelengths ($\lambda \gg M$) will simply reflect through the origin as if the black hole were not present.

Of course it is impossible to construct a strictly ingoing pulse since the scalar field will back-scatter from its own gravitational potential. However, we can get a nearly ingoing pulse using the following method.

Let $\phi\left(r, t\right) = F\left(u \equiv r + t\right)/r$. Since the ingoing characteristic speed is one, u is an ingoing coordinate. Thus, $\dot{\phi} = \partial_u F/r$ and $\phi' = \partial_u F/r - F/r^2$. For a compact pulse we set F to a Gaussian of the form

$$F\left(u\right) = Au^2 \exp\Big(- \left(u-c\right)^d/\sigma^d\Big), \tag{3.4.1}$$

where d is an integer and c is the r coordinate of the center of the pulse. This results in initial data for ϕ of the form

$$\phi\left(r\right) = Ar \exp\Big(- \left(r-c\right)^d/\sigma^d\Big), \tag{3.4.2}$$

$$\phi'\left(r\right) = \phi\Big[\frac{1}{r} - \frac{d}{\sigma^d}\left(r-c\right)^{d-1}\Big], \tag{3.4.3}$$

and

$$\dot{\phi}(r) = \phi\Big[\frac{2}{r} - \frac{d}{\sigma^d}\left(r-c\right)^{d-1}\Big]. \tag{3.4.4}$$

These equations can be used to set Φ and Π. I solve for β, a, and $K^{\theta}{}_{\theta}$ using equations (3.2.5), (3.2.10), and (3.2.11), respectively. $K^{r}{}_{r}$ can be specified freely and the constraints can still be

satisfied by adjusting the other geometric variables. However, an arbitrary $K^r{}_r$ would almost certainly not represent the desired configuration of a scalar field around a black hole.

I tried a number of methods for setting $K^r{}_r$, including finding the initial data in polar-radial coordinates and then transforming to MMIEF coordinates. However, because of the different slicings, one MMIEF slice crosses many polar-radial slices. This requires that the data be evolved in the polar-radial system for enough time so that the initial MMIEF slice is covered. I elected to use a different approach which seems to give good results. I use the Schwarzschild form (3.2.27) for $K^r{}_r$, but with varying mass. That is, I solve for $M(r)$ (3.2.30) along with the constraints and then substitute this mass profile into (3.2.27) in place of the black hole mass M.

3.5. Tails

There are a number of physical effects that we can expect to observe during the scattering of the scalar field. The first of these is the so-called power law tails (see [10] and [19]). This effect is due completely to the curvature and would occur around any mass. What happens is that outgoing radiation is back-scattered by the curvature and reaches the interior at late times. This causes the scalar field at the horizon or any fixed areal radius to fall off as a power of time, independent of the shape of the scattered pulse (see [11]).

According to this reference, given Gaussian initial data, we should expect the scalar field to go like t^{-3} at fixed areal radius and like v^{-3} at the horizon, where t is time at infinity, $v \equiv t + r^*$ is the advanced time, and

$$r^* \equiv r + 2M\ln\left(r - 2M\right) \tag{3.5.1}$$

is the "tortoise" coordinate. In MMIEF coordinates, v varies like t at the horizon, so we should expect the scalar field to fall off like t^{-3} at both the horizon and fixed areal radius.

3.6. Ringing

Another effect we should observe is *quasi-normal ringing.* This effect was observed from studying perturbations on a fixed Schwarzschild background [20]. If the perturbation field Φ is written as a sum of spherical harmonics

$$\Phi = \sum_l \frac{1}{r} \Psi_l(t,r)\, Y_{lm}(\theta,\phi)\,, \tag{3.6.1}$$

then the radial part will obey the Regge-Wheeler equation

$$\left(-\partial_t^2 + \partial_{r^*}^2\right)\Psi_l = V_{eff}(r)\,\Psi_l\,. \tag{3.6.2}$$

r^* is defined by (3.5.1). (3.6.2) is just a one dimensional flat-space wave equation with an effective potential

$$V_{eff}(r) \;=\; \left(1-\frac{2M}{r}\right)\left(\frac{l(l+1)}{r^2}+\frac{2Mq}{r^3}\right), \tag{3.6.3}$$

where $q = -3,\, 0,\, 1$ for gravitational, electromagnetic, or scalar perturbations, respectively [15].

When waves impinge on the black hole, the perturbation field will oscillate at certain frequencies which depend only on the mass of the black hole. These frequencies can be found from the poles of the scattering amplitude (see [15] for a detailed treatment). The half-period for an oscillation due to a spherical scalar perturbation is $28.44M$ [12].

3.7. Mass Scaling

The final mass of the black hole should scale as a power of the initial amplitude of the scalar field. To find out what this power should be, we can use equation (3.2.30) which gives the mass as an integral of the scalar field. If we take the integral throughout space (neglecting the potential V), we get

$$M_\infty = M_h + 4\pi \int_{r_h}^{\infty} s^2 \left(\frac{\Phi^2 + \Pi^2}{2a^2} + sK^\theta{}_\theta \frac{\Phi\Pi}{a} \right) dr, \tag{3.7.1}$$

where $M_h \equiv \frac{s_h}{2}$ is the mass of the black hole. Since the mass is conserved, M_∞ is a constant. However, M_h is not constant. As the scalar field encounters the horizon, some mass will be transferred from the integral term to M_h. The mass of the black hole will increase by an amount proportional to the mass in the scalar field. For a very narrow pulse, the entire mass of the field will go into the black hole, while for a very wide pulse, almost none of it will. So, to see how the final mass of the black hole scales with the amplitude of the scalar pulse, we need only examine the integral term in equation (3.7.1).

The initial data is given by equations (3.4.2) , (3.4.3), and (3.4.4). Using these along with equations (3.1.13) and (3.1.14), we get

$$\Phi = \phi \left[\frac{1}{r} - \frac{d\left(r-c\right)^{d-1}}{\sigma^d} \right] \tag{3.7.2}$$

and

$$\Pi = \phi \left[\frac{2-\beta}{r\left(1-\beta\right)} - \frac{d\left(r-c\right)^{d-1}}{\sigma^d} \right]. \tag{3.7.3}$$

Thus, Φ and Π are both proportional to ϕ and hence to A. This means that the integrand is proportional to ϕ^2 and thus to A^2. Now this assumes that the dependence of a, $K^\theta{}_\theta$, and β on ϕ is much less than the dependence of M on ϕ which seems a reasonable assumption. However, the mass scaling will be easy to check numerically. If it turns out that $M \propto A^2$ then we know this assumption is valid.

Chapter 4. Spherical Symmetry II: Massless Scalar Field

4.1. Finite Difference Equations

I will solve equations (3.2.10) - (3.2.20) using finite difference techniques on a uniform mesh with spacings Δr and Δt.

Table 4.1 shows the operators I will use in the discretizations. Note that while the derivative operators take a lower precedence than the arithmetic operators, that is $\triangle_r f_i^{n2} = \left(f_{i+1}^{n\ 2} - f_{i-1}^{n\ 2}\right)/\Delta r$, the time averaging operator takes a higher precedence, that is $A_t f_i^{n2} = \left(A_t f_i^n\right)^2$ and $A_t\left(a_i^n b_i^n\right) = A_t a_i^n A_t b_i^n$.

I initially intended to use a free evolution scheme for this set of equations, but was unable to difference equation (3.2.14) in a stable way. Thus, I use equations (3.2.12), (3.2.13), (3.2.15), (3.2.16), and (3.2.20) to evolve $a, K^\theta{}_\theta, \Phi, \Pi,$ and f; equation (3.2.11) to find $K^r{}_r$; and equation (3.2.5) to find β.

In the interior, I use the following finite difference equations:

$$\triangle_t^d a_i^n = -A_t\left(a^2\left(1-\beta\right)\right)_i^n + \triangle_r^s\left(a\beta\right)_i^n, \tag{4.1.1}$$

$$\triangle_t^d K^\theta{}_{\theta_i}{}^n = A_t\beta_i^n \triangle_r^s K^\theta{}_{\theta_i}{}^n + A_t\left(\frac{1-\beta}{s^2}\left(a-\frac{1}{a}\right)\right)_i^n + \frac{\triangle_r^a \beta_i^n}{A_t\left(as\right)_i^n}$$

$$+ A_t\left(a\left(1-\beta\right)K^\theta{}_\theta\left(2K^\theta{}_\theta + K^r{}_r\right)\right)_i^n, \tag{4.1.2}$$

Operator	**Definition**	**Expansion**
$\triangle_r^f f_i^n$	$\left(-3f_i^n + 4f_{i+1}^n - f_{i+2}^n\right)/2\Delta r$	$\left.\frac{\partial f}{\partial r}\right\|_i^n + O\left(\Delta r^2\right)$
$\triangle_r^b f_i^n$	$\left(3f_i^n - 4f_{i-1}^n + f_{i-2}^n\right)/2\Delta r$	$\left.\frac{\partial f}{\partial r}\right\|_i^n + O\left(\Delta r^2\right)$
$\triangle_r f_i^n$	$\left(f_{i+1}^n - f_{i-1}^n\right)/2\Delta r$	$\left.\frac{\partial f}{\partial r}\right\|_i^n + O\left(\Delta r^2\right)$
$\triangle_t f_i^n$	$\left(f_i^{n+1} - f_i^n\right)/\Delta t$	$\left.\frac{\partial f}{\partial t}\right\|_i^{n+½} + O\left(\Delta t^2\right)$
$\triangle_t^d f_i^n$	$\left(f_i^{n+1} - f_i^n\right)/\Delta t +$	$\left.\frac{\partial f}{\partial t}\right\|_i^{n+½} + O\left(\Delta t^2\right)$
	$\varepsilon_{dis}\Big[6f_i^n + f_{i-2}^n + f_{i+2}^n -$	
	$\left(f_{i-1}^n + f_{i+1}^n\right)\Big]/16\Delta t$	
$A_t f_i^n$	$\left(f_i^{n+1} + f_i^n\right)/2$	$f\mid_i^{n+½} + O\left(\Delta t^2\right)$
$A_r f_i^n$	$\left(f_i^n + f_{i-1}^n\right)/2$	$f\mid_{i-½}^n + O\left(\Delta r^2\right)$
$\triangle_r^{fa} f_i^n$	$A_t \triangle_r^f f_i^n$	$\left.\frac{\partial f}{\partial r}\right\|_i^{n+½} + O\left(\Delta r^2 + \Delta t^2\right)$
$\triangle_r^{ba} f_i^n$	$A_t \triangle_r^b f_i^n$	$\left.\frac{\partial f}{\partial r}\right\|_i^{n+½} + O\left(\Delta r^2 + \Delta t^2\right)$
$\triangle_r^a f_i^n$	$A_t \triangle_r f_i^n$	$\left.\frac{\partial f}{\partial r}\right\|_i^{n+½} + O\left(\Delta r^2 + \Delta t^2\right)$
$\triangle_r^s f_i^n$	$\left(f_i^{n+1} - f_{i-1}^{n+1} + f_{i+1}^n - f_i^n\right)/2\Delta r$	$\left.\frac{\partial f}{\partial r}\right\|_i^{n+½} + O\left(\Delta r^2 + \Delta t^2 + \Delta r\Delta t\right)$

Table 4.1. Two-Level Finite Difference Operators

$$A_t\left(\triangle_r K^\theta{}_\theta + \frac{K^\theta{}_\theta - K^r{}_r}{s} - 4\pi\frac{\Phi\Pi}{a}\right)_i^n = 0, \tag{4.1.3}$$

$$\triangle_t^d \Phi_i^n = \triangle_r^s \left(\beta \Phi + \left(1-\beta\right) \Pi \right)_i^n, \tag{4.1.4}$$

$$\triangle_t^d \Pi_i^n = \frac{1}{A_t \left(s_i^n\right)^2} \triangle_r^s \left(s^2 \left(\beta \Pi + \left(1-\beta\right) \Phi \right) \right)_i^n - 2 \triangle_t s_i^n A_t \left(\frac{\Pi}{s} \right)_i^n, \tag{4.1.5}$$

$$\triangle_t f_i^n = 4\pi A_t \left(\frac{s_i^n \left(\Phi_i^n + \Pi_i^n \right)}{a_i^n} \right)^2, \tag{4.1.6}$$

$$s_i^{n+1} = r_i + f_i^{n+1}, \tag{4.1.7}$$

$$A_t \beta_i^n = \frac{\triangle_t f_i^n + A_t \left(asK^\theta{}_\theta \right)_i^n}{1 + A_t \left(asK^\theta{}_\theta \right)_i^n}. \tag{4.1.8}$$

These equations are applied everywhere in the interior except at the two points next to the boundary points. At these points, I use the same equations except the dissipative time derivatives, $\triangle_t^d$ are replaced by regular time derivatives, $\triangle_t$ since the value at $i+2$ or $i-2$ is not available at these locations. It is interesting to note that all of the spatial derivatives are *angled* ($\triangle_r^s$) except for the derivative of β in equation (4.1.2) and the derivative of $K^\theta{}_\theta$ in equation (4.1.3). Switching any of these derivatives from angled to non-angled or from non-angled to angled results in an instability.

The inner boundary is fixed to the apparent horizon. Thus, there is no physical condition available for the evolution equations. Rather, due to the tipping of the light cones, the function values on the horizon can be advanced using only the points outside the black hole. Therefore, I use the same equations as I use in the interior, except the centered derivatives are replaced by forward derivatives. For example, equation (4.1.1) becomes

$$\triangle_t a_i^n = -A_t \left(a^2 \left(1-\beta\right) \right)_i^n + \triangle_r^a \left(a\beta \right)_i^n. \tag{4.1.9}$$

Since the computational grid must be finite, the outer boundary can not be extended to infinity. I adopt outgoing conditions at the outer boundary, that is, I assume that no radiation

will enter the grid from large r. While this is not strictly true (there will be curvature back-scattering from the outgoing pulse), it provides a good computational solution.

For the scalar field variables Φ and Π, the outgoing conditions come from the condition on ϕ, namely $s\phi \sim F\left(s-ct\right)$, with $c = 1-2\beta$ being the speed of outgoing waves. This means that

$$\dot{\Phi} + \left(1-2\beta\right)\Phi' + \frac{\left(\dot{s}+1-2\beta-2s\beta'\right)}{s}\Phi - \frac{\left(\dot{s}+1-2\beta+2s\beta'\right)}{s^2}\phi = 0 \qquad (4.1.10)$$

and

$$\left(1-\beta\right)\left(\Pi+\Phi\right) + \frac{\left(1-2\beta\right)+\dot{s}}{s}\phi = 0. \qquad (4.1.11)$$

These equations are discretized as

$$\triangle_t \Phi_i^n + \left(1-2A_t\beta_i^n\right)\triangle_r^b \Phi_i^n + \frac{\triangle_t s_i^n + 1 - 2A_t\beta_i^n - 2A_t s_i^n \triangle_r^b \beta_i^n}{A_t s_i^n} A_t \Phi_i^n$$

$$- \frac{\triangle_t s_i^n + 1 - 2A_t\beta_i^n + 2A_t s_i^n \triangle_r^b \beta_i^n}{\left(A_t s_i^n\right)^2} A_t \phi_i^n = 0 \qquad (4.1.12)$$

and

$$A_t\left[\left(1-\beta\right)\left(\Pi+\Phi\right)\right]_i^n + \frac{1-2A_t\beta_i^n+\triangle_t s_i^n}{A_t s_i^n} A_t\phi_i^n = 0. \qquad (4.1.13)$$

We can get approximate conditions on a and $K^\theta{}_\theta$ from their Schwarzschild forms (3.2.25) and (3.2.26) and the integral expression for the mass (3.2.30). Outside of any matter (very weak scalar field), a and $K^\theta{}_\theta$ should take on their Schwarzschild forms. For large s we can take asymptotic expansions of these to get

$$a \sim 1 + \frac{M}{s} + O\left(s^{-2}\right) \qquad (4.1.14)$$

and

$$K^{\theta}{}_{\theta} \sim \frac{2M}{s^2} + O\left(s^{-3}\right) \tag{4.1.15}$$

Thus, at large r we have basically

$$s\left(a-1\right) \sim M \tag{4.1.16}$$

and

$$s^2 K^{\theta}{}_{\theta} \sim M. \tag{4.1.17}$$

Now how does M behave in the large s weak-field limit? Since $a \to 1$ and $K^{\theta}{}_{\theta} \to 0$ we have

$$M \sim 4\pi \int s^2 \left(\Phi^2 + \Pi^2\right) ds\,. \tag{4.1.18}$$

From the condition on ϕ we can see that $\Phi \sim G\left(u\right)/s$ and $\Pi \sim G\left(u\right)/s$, where $u \equiv s - c\,t$. Thus

$$M \sim 8\pi \int G^2\left(u\right) du \sim H\left(U\right), \tag{4.1.19}$$

that is, M is "outgoing" at large s. Therefore we get the following conditions for a and $K^{\theta}{}_{\theta}$

$$s\left(a-1\right) \sim H\left(s-ct\right) \tag{4.1.20}$$

and

$$s^2 K^{\theta}{}_{\theta} \sim H\left(s-ct\right). \tag{4.1.21}$$

These are discretized as

$$\triangle_t \left(s\left(a-1\right)\right)^n_i + \left(1 - 2A_t\,\beta^n_i\right) \triangle^b_r \left(s\left(a-1\right)\right)^n_i = 0 \tag{4.1.22}$$

and

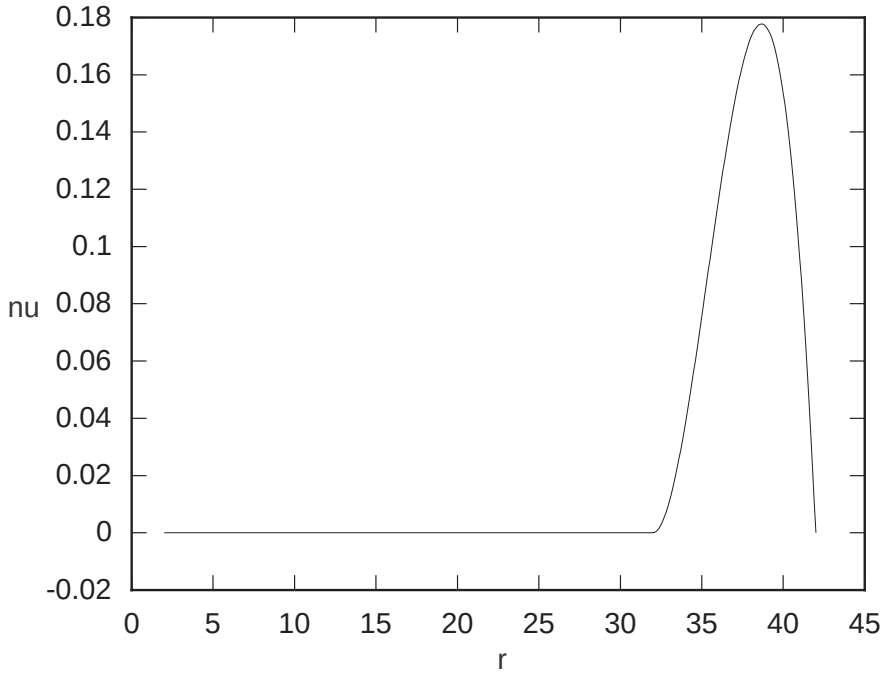

Figure 4.1. Sponge filter coefficient function for $A = 1.0$ and $n = 2$.

$$\triangle_t \left(s^2 K^\theta{}_\theta\right)_i^n + \left(1 - 2A_t \beta_i^n\right) \triangle_r^b \left(s^2 K^\theta{}_\theta\right)_i^n = 0. \tag{4.1.23}$$

The outgoing boundary condition reduces the amplitude of reflections off the boundary, but unless the boundary is placed at very large r, these reflections can still interfere with the results of a calculation. To minimize the reflections, I use a *sponge filter* as detailed in [6]. This means that in the interior of the grid, I apply the usual evolution equation along with a coefficient times the outgoing condition. For instance, in the case of Φ, the equation is

$$\dot{\Phi} = \left(\beta\Phi + \left(1-\beta\right)\Pi\right)' - \nu\left[\dot{\Phi} + \left(1-2\beta\right)\Phi' + \frac{\dot{s} + 1 - 2\beta - 2s\beta'}{s}\Phi - \frac{\dot{s} + 1 - 2\beta + 2s\beta'}{s^2}\phi\right], \tag{4.1.24}$$

where $\nu(r)$ is the coefficient function given by

$$\nu(r) = \begin{cases} 0 & r_{\min} \le r < r_s \\ A(r-r_s)^n (r_{\max}-r)\,(r_{\max}-r_s)^{-n-2}(n+1)\,(n+2) & r_s \le r < r_{\max} \end{cases}. \tag{4.1.25}$$

Here, A and n are parameters. Figure 4.1 shows ν for $A = 1.0$ and $n = 2$, the values used in this thesis.

4.2. Initial Data

Section 3.4 gives the equations used to compute the initial data. These equations are solved using an iterative procedure. First, the scalar field is set to an "ingoing" pulse (see Section 3.4) and the geometric variables are set to their Schwarzschild values (see Section 3.2). Then a and $K^{\theta}{}_{\theta}$ are integrated from equations (3.2.10) and (3.2.11). Using these, the new forms of $M(r)$ and β are computed. Finally, $K^{r}{}_{r}$ is computed. The program then computes a and $K^{\theta}{}_{\theta}$ again and so on until each of the geometric functions converges to a final value. In practice, this takes about twenty iterations.

The resulting initial data is shown in Figures 4.2 and 4.3. It seems to behave as a strictly ingoing pulse, however, it may contain an outgoing piece which only shows up at large amplitudes (see Section 4.6).

4.3. Tails

Figure 4.4 shows ϕ at constant r for runs with $r_{\max} = 42,\ 82,\ 162$. It is clear that the position of the outer boundary has a large effect on the fall-off of the scalar field, even with the sponge filter. There is enough reflection to cause the field to fall off much more slowly than it should. In order to accurately measure the tails, it would be necessary to either use an adaptive scheme so that the boundary can be moved out to several thousand M, or to match the interior evolution to a characteristic scheme which would evolve the region of spacetime from the boundary to spatial infinity.

However, with the outer boundary at $r_{\max} = 162$, it will take at least $300M$ for reflections from the scattered pulse to travel in from the outer boundary and interfere with measurements

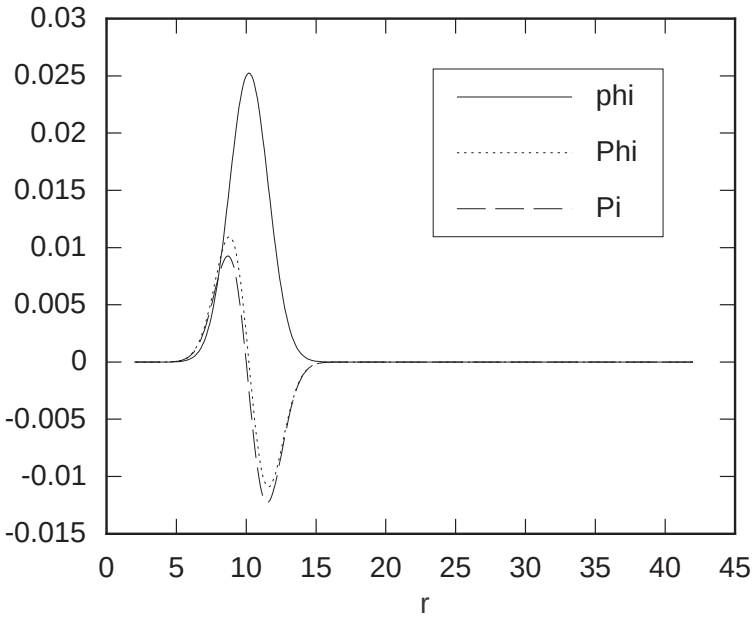

Figure 4.2. Initial data for the scalar field with $A = 3.0 \times 10^{-3}$, $c = 10$, and $\sigma = 2$.

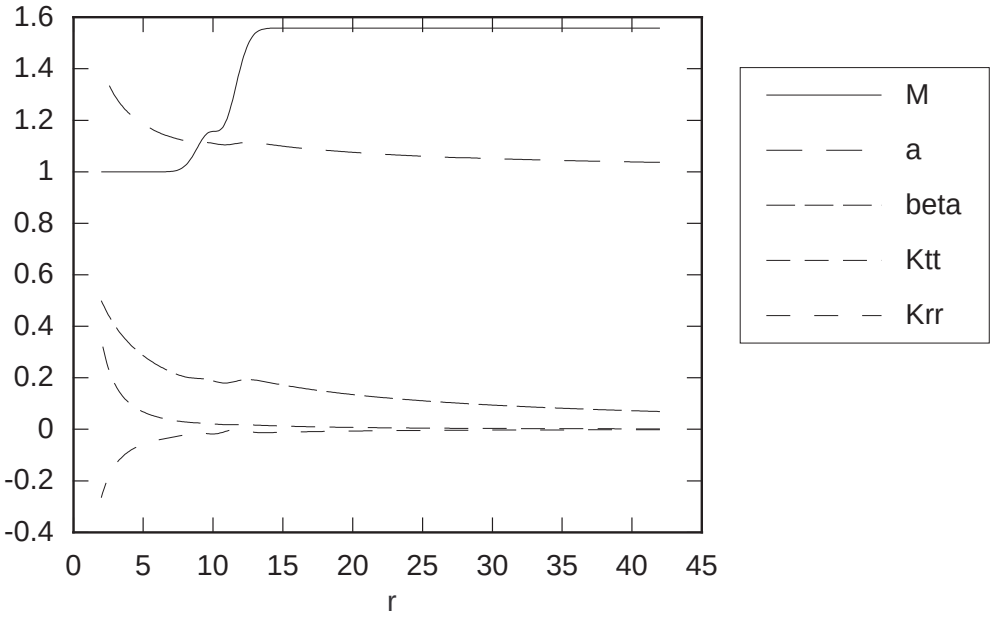

Figure 4.3. Initial data for the geometric variables and the mass profile with $A = 3.0 \times 10^{-3}$, $c = 10$, and $\sigma = 2$.

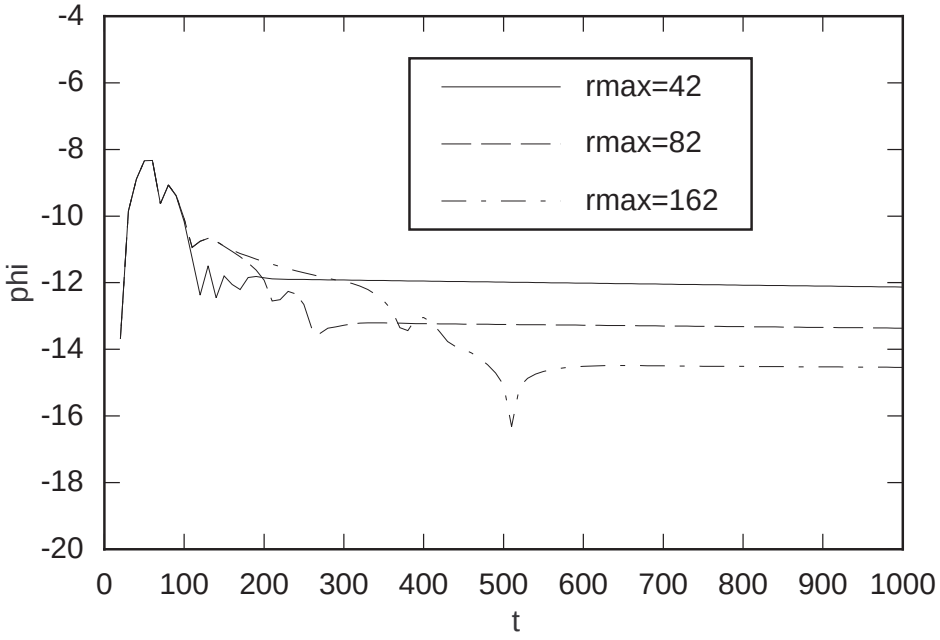

Figure 4.4. $\log\left|\phi\right|$ at $r = 30$ verses t for various spatial domains.

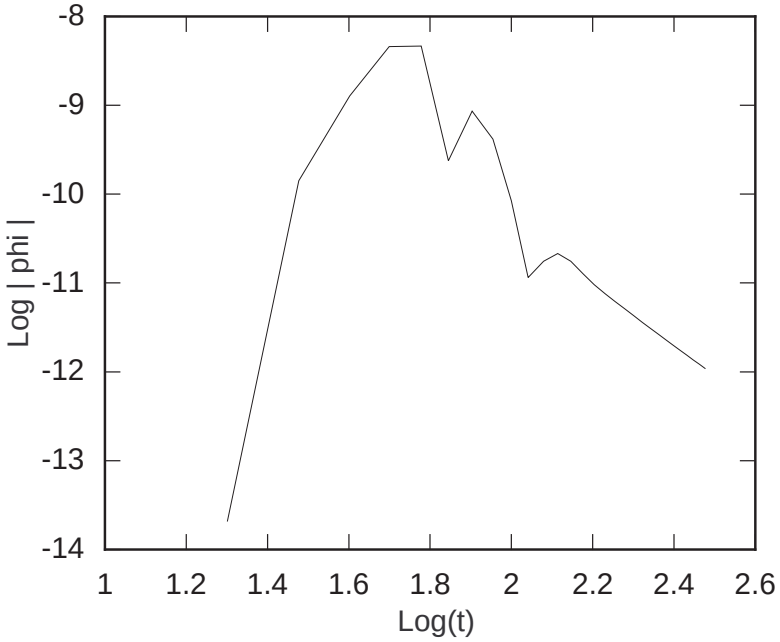

Figure 4.5. $\log\left|\phi\right|$ at $r = 30$ verses $\log t$.

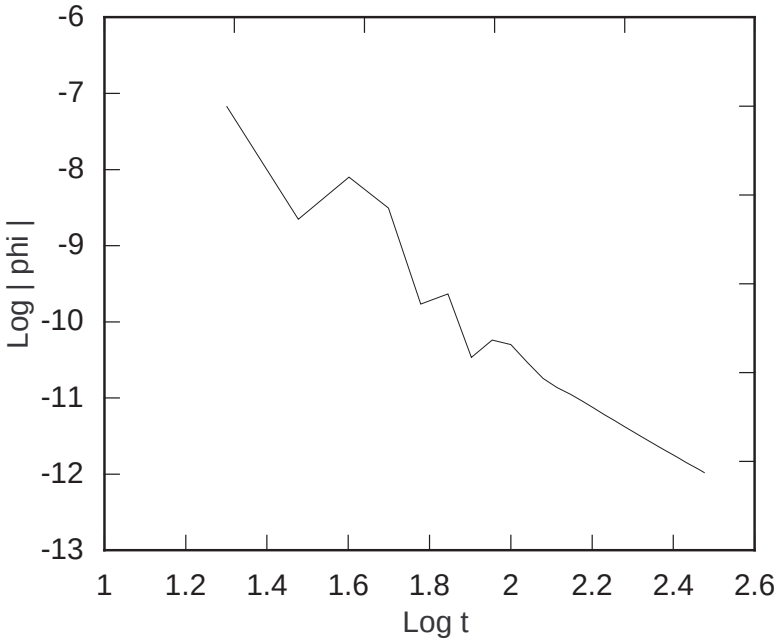

Figure 4.6. $\log|\phi|$ at the horizon verses $\log t$.

at $r = 30$. This should give enough time to measure the rate of fall off of the scalar field. Figure 4.5 shows the accurate part of the evolution. A fit to this curve between $200\,M$ and $300\,M$ shows ϕ falling off as $t^{-3.38}$. A run at twice the resolution yields the same exponent.

The evolution of ϕ at the horizon is shown in Figure 4.6. A linear fit to this curve between $200\,M$ and $300\,M$ shows ϕ falling off as $t^{-3.06}$ for runs at both resolutions.

4.4. Ringing

Figure 4.7 shows the waveforms generated by packets of various widths for medium field data ($.017M \leq M_{\phi} \leq .052M$). This graph shows the initial pulse of reflected scalar field. Figure 4.8 shows $\log|\phi|$ at the horizon for the same data. In this graph the subsequent oscillations are apparent. It is also apparent that the frequency is independent of the pulse width. The period for one oscillation is approximately $53\,M$ giving a half-period of $26.5M$ which is close to the predicted value of $28.44M$. A Higher resolution run with the same data yields a half-period of $26.25M$.

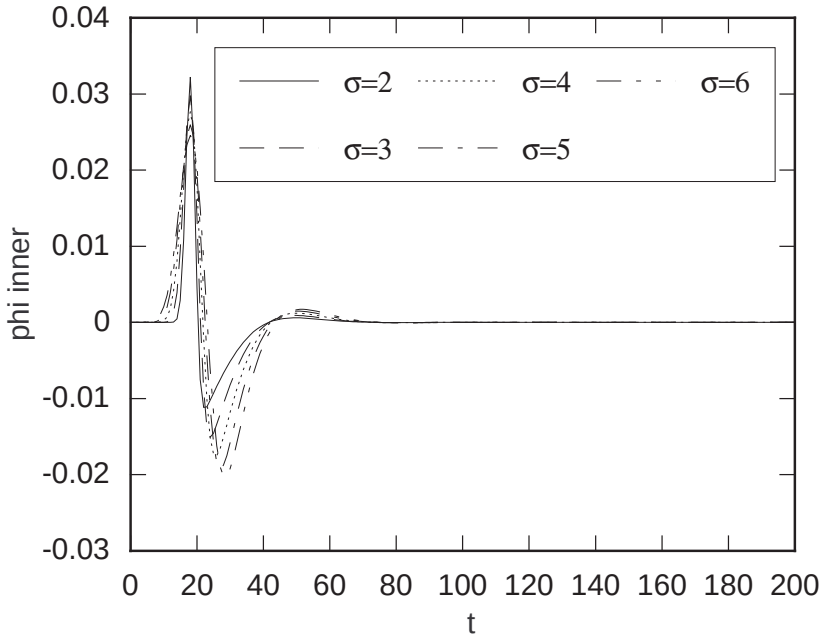

Figure 4.7. ϕ at the horizon verses time for various pulse widths ($A = 2.0 \times 10^{-4}$).

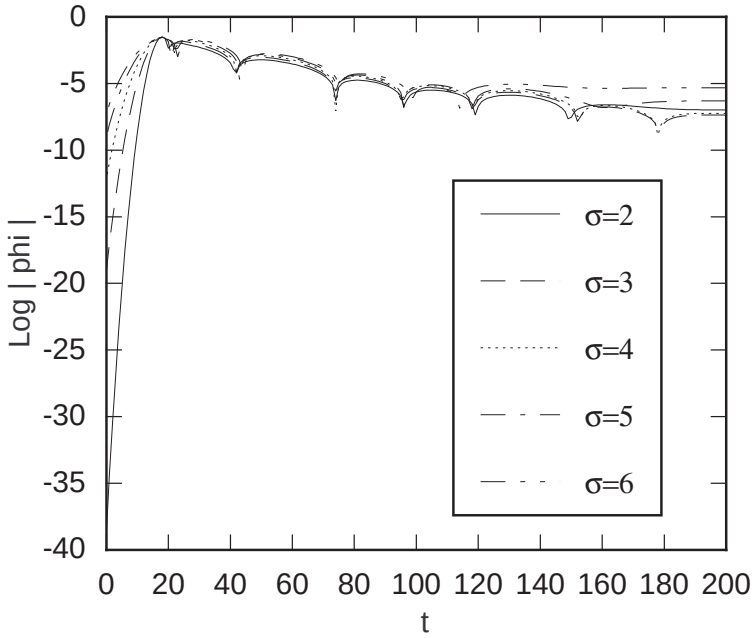

Figure 4.8. $\log\left|\phi\right|$ at the horizon verses time for various pulse widths ($A = 2.0 \times 10^{-4}$).

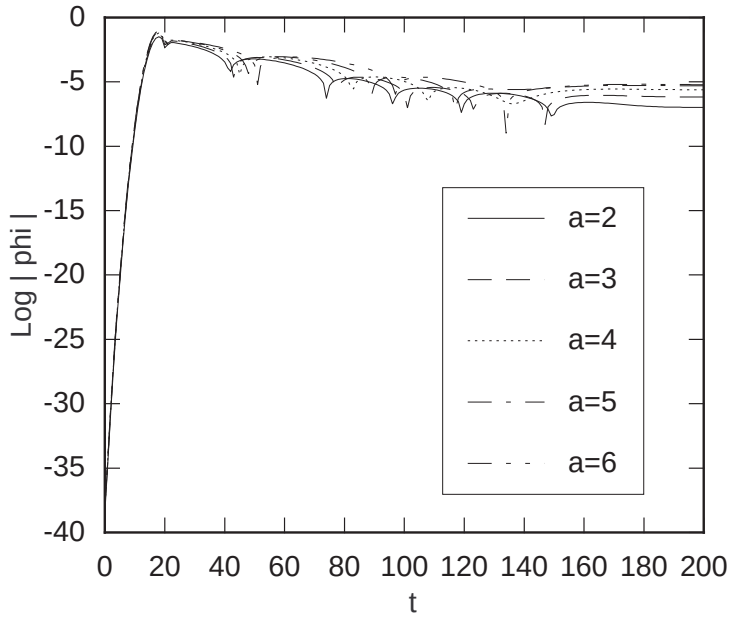

Figure 4.9. $\log|\phi|$ at the horizon verses time for various pulse amplitudes ($\sigma = 2.0$, amplitudes are $\times 10^{-4}$).

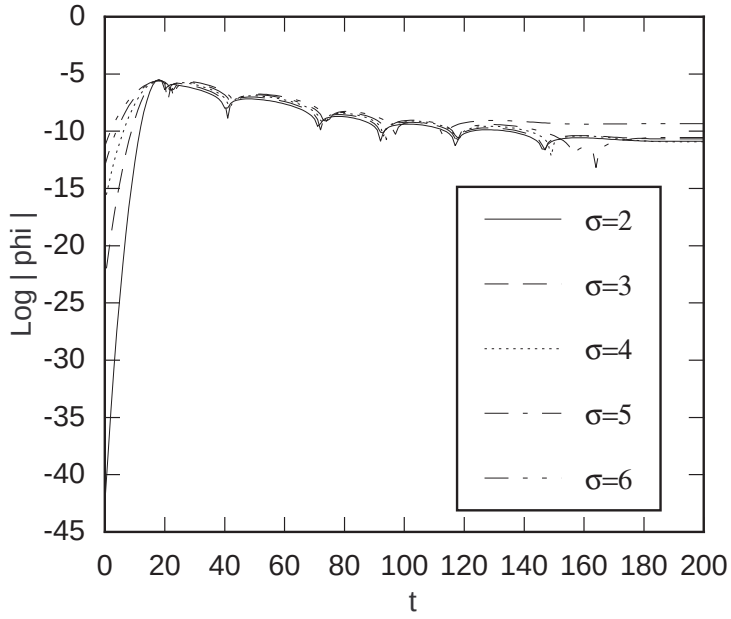

Figure 4.10. $\log|\phi|$ at the horizon verses time for various pulse widths ($A = 2.0 \times 10^{-8}$).

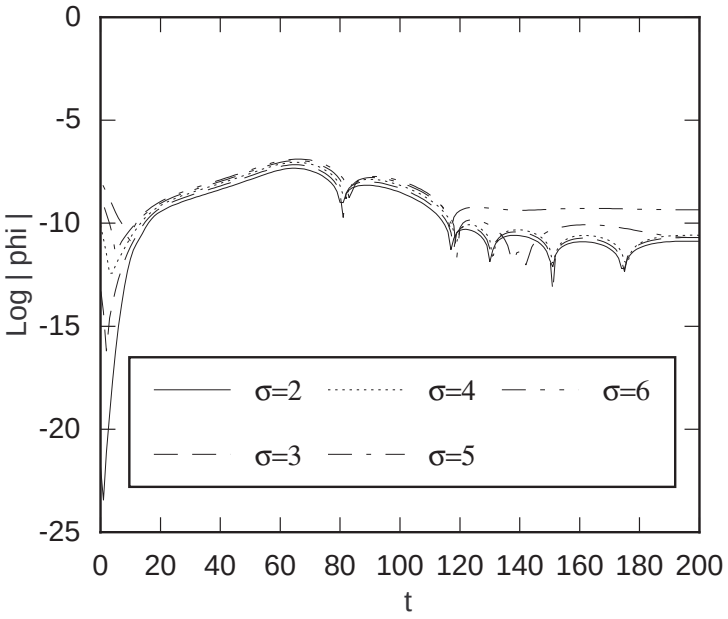

Figure 4.11. $\log|\phi|$ at $r = 30$ verses time for various pulse widths ($A = 2.0 \times 10^{-8}$).

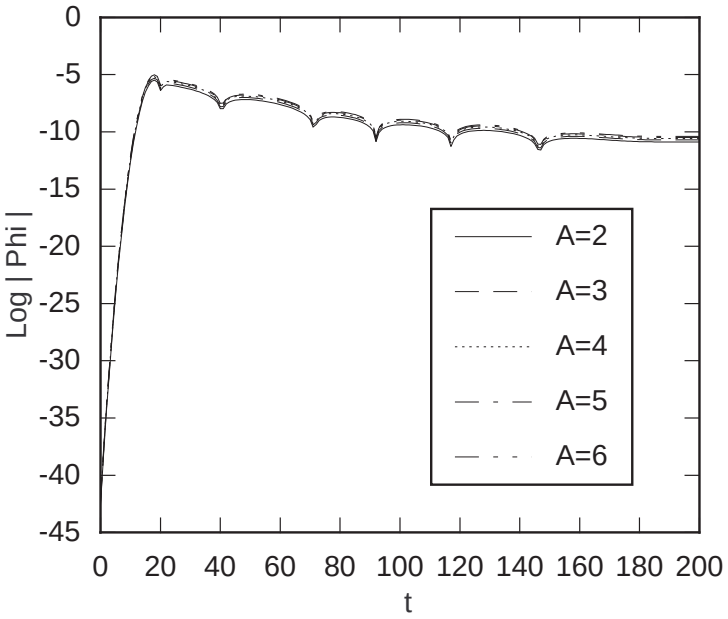

Figure 4.12. $\log|\phi|$ at the horizon verses time for various pulse amplitudes ($\sigma = 2.0$, amplitudes are $\times 10^{-8}$).

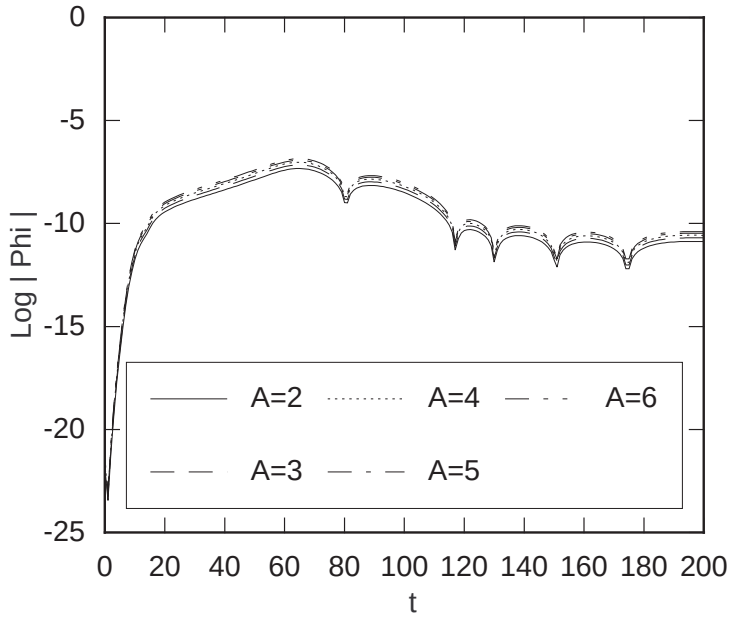

Figure 4.13. $\log|\phi|$ at $r = 30$ verses time for various pulse amplitudes ($\sigma = 2.0$, amplitudes are $\times 10^{-8}$).

Figure 4.9 shows the waveforms generated by pulses of varying amplitude for strong field data ($.051M \leq M_{\phi} \leq .47M$). In this case, the frequency of oscillations decreases with increasing amplitude. However, the mass of the black hole changes from 1.0 to 1.46 during the evolution of the strongest data, so the period is expected to increase.

The weak-field data shown in Figures 4.10–4.13 gives an oscillation period of approximately $53M$. This period is independent of the initial pulse amplitude as expected. For large widths, the late-time waveform differs from that of a small width. As the width becomes larger, less and less of the initial pulse is absorbed by the black hole. This means there is more scalar field available to be reflected from the outer boundary and cause differences in the late-time evolution at fixed radius.

4.5. Mass Scaling

The infalling scalar field can exhibit two main behaviors depending on the amplitude and width of the pulse. These are: *scattering* from the existing black hole and *collapse* to form

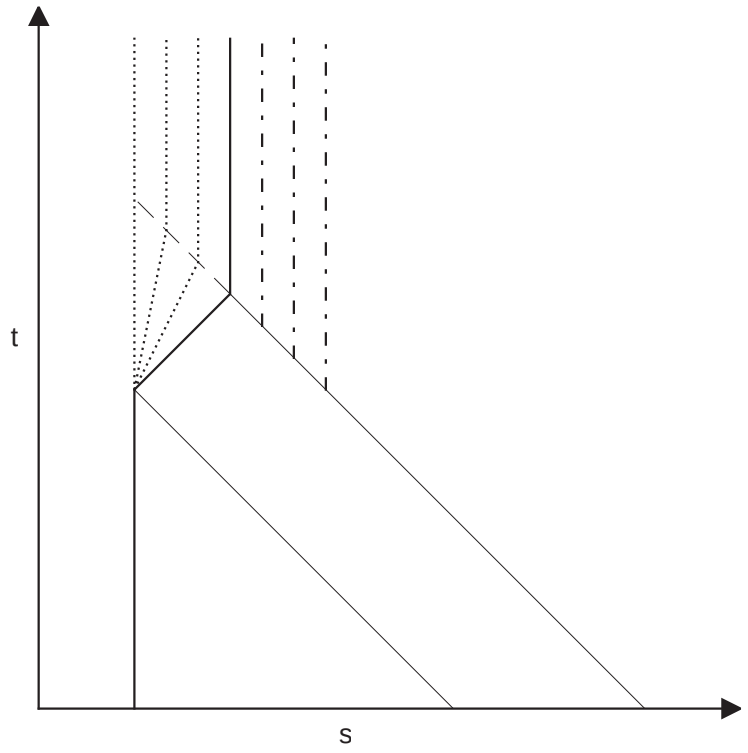

Figure 4.14. Schematic motion of the horizon for various amplitudes of the scalar field.

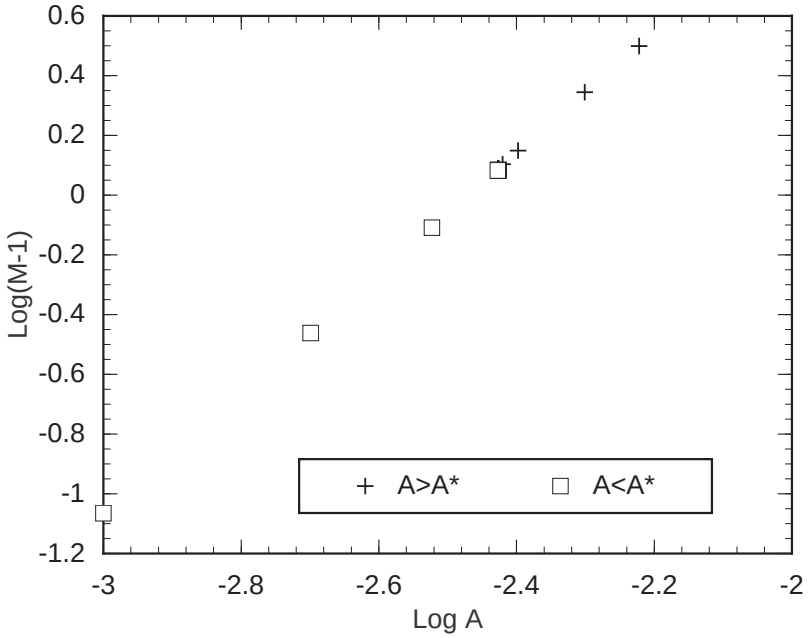

Figure 4.15. Final black hole mass verses amplitude of the scalar field pulse ($d = 2$).

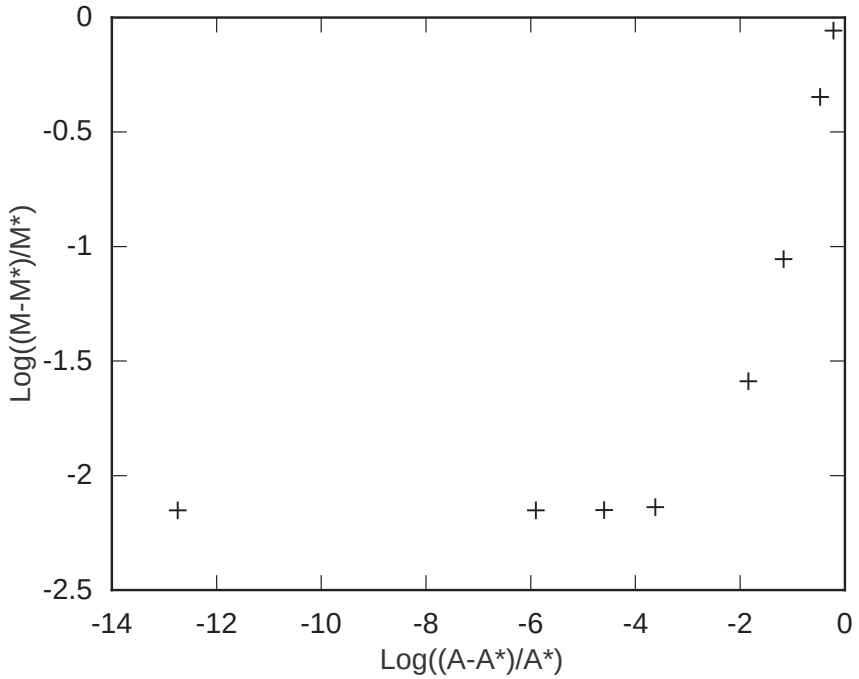

Figure 4.16. Final black hole mass verses amplitude of the scalar field pulse ($d = 2$) for super-critical amplitudes.

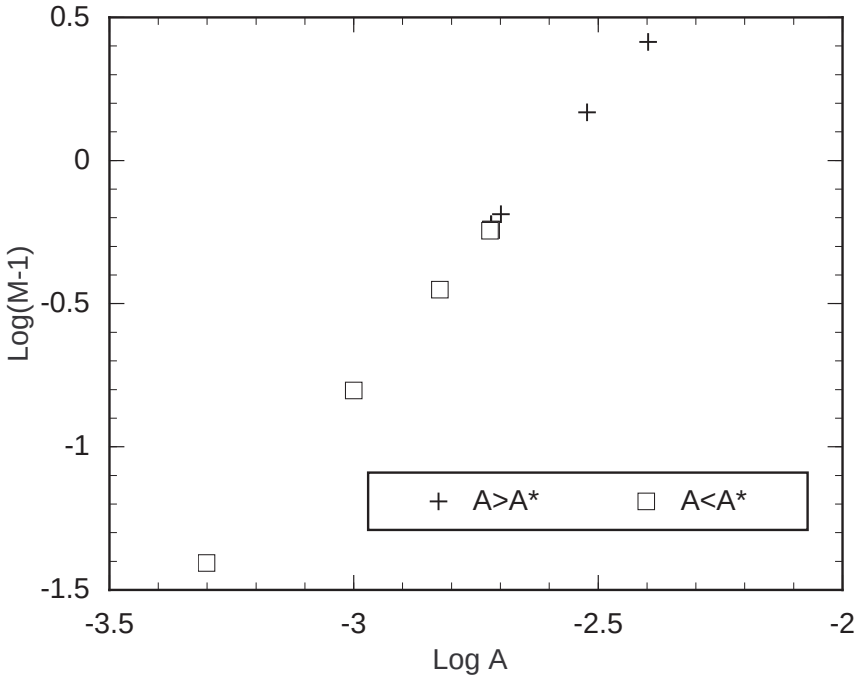

Figure 4.17. Final black hole mass verses amplitude of the scalar field pulse ($d = 4$).

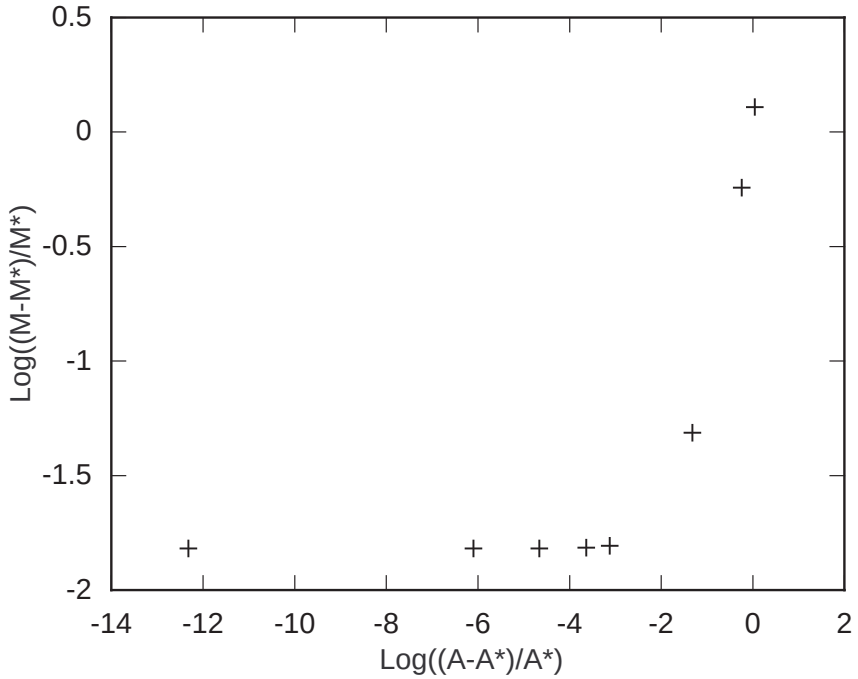

Figure 4.18. Final black hole mass verses amplitude of the scalar field pulse ($d = 4$) for super-critical amplitudes.

a new horizon outside the existing horizon. These two behaviors are separated by a *critical* value of either amplitude or width. For initial data with $\sigma = 2$, $c = 10$, and $d = 2$, the critical amplitude is $A \approx .0037$, while for initial data with $d = 4$, the critical amplitude is $A \approx .0019$.

Figure 4.14 shows a spacetime diagram of the motion of the horizon for various amplitudes of initial data. Notice that this diagram uses the areal coordinate s and not the radial coordinate r. The solid dark vertical line which jogs right and then continues vertically represents the critical path of the horizon. The dotted lines are sub-critical paths and the vertical dashed lines are super-critical paths. The two thin, diagonal lines represent the bounds of the ingoing pulse of scalar field. A super-critical pulse moves inward until it crosses its gravitational radius. Once this happens, the apparent horizon jumps from its initial position to this new position where it remains. A sub-critical pulse moves inward until it encounters the horizon. If the field is very weak, the horizon is unaffected. For stronger fields, the horizon moves out until the pulse is entirely inside. For a critical pulse, the horizon moves out at the

speed of light. Note however, that unless the energy density is a square wave, the horizon will not move along the straight lines as shown in the diagram, but will move along a curve with gradually increasing and then decreasing slope.

The final mass of the black hole should scale with the amplitude of the initial data as shown in Section 3.7. If the picture in Figure 4.14 is correct, both super-critical and sub-critical data should exhibit the same mass scaling. Figure 4.15 shows $\log\left(M-1\right)$ verses A for initial data with $d=2, \sigma=2$, and $c=10$. The squares are for data with amplitude less than the critical value, while those with crosses are for data with amplitude greater than the critical value. This graph is fit by the line

$$\log\left(M-1\right) = 2.01\log A + 4.96, \tag{4.5.1}$$

indicating that the mass grows with the square of the amplitude as expected. The graph also shows there is no difference in behavior for sub- and super-critical data. That is, the final mass of the black hole exhibits the same dependence on the amplitude when the hole grows by accretion or when it forms by collapse.

Figure 4.16 shows only super-critical data. The mass values are asymptoting to $M \approx 2.22$ indicating a mass gap between the smallest super-critical black hole and the largest sub-critical black hole. In fact, the super-critical mass is $M_+ = 2.2281725$ while the sub-critical mass is $M_- = 2.2125908$. This effect is purely numerical. The method for solving the difference equations demands that the horizon be located on a grid point. The radial distance between grid points, Δr is also the areal distance Δs. The mass of the black hole is $s_h/2$ (see equation (3.2.30)). Now the location of the horizon should be accurate to within $\Delta r/2$. Thus, we would expect the mass gap to be approximately $\Delta r/4$. The data plotted in the figures was computed on a grid with $\Delta r = .1$. Thus, the mass gap should be about $\Delta M \approx .025$. The actual mass gap is about .0155. For a grid with $\Delta r = .05$ we get $M_+ = 2.316354$ and $M_- = 2.309658$ for a difference of $\Delta M \approx .0067$, while a grid with $\Delta r = .025$ gives $M_+ = 2.3660016, M_- = 2.3635547$, and $\Delta M \approx .0024$.

Figures 4.17 and 4.18 show similar behavior for data with $d=4$. Figure 4.17 is fit by the line

$$\log\left(M-1\right) = 1.99\log A + 5.19, \tag{4.5.2}$$

indicating again that the mass grows with the square of the amplitude.

Figure 4.18 again shows a mass gap. Of course this too is numerical and shrinks with the grid spacing. The grid with $\Delta r = .1$ gives $\Delta M \approx .024$, the grid with $\Delta r = .05$ gives $\Delta M \approx .006$, and the grid with $\Delta r = .025$ gives $\Delta M \approx .002$.

4.6. Coordinate Effects

The evolutions exhibit some interesting effects which are due to the use of MMIEF coordinates. The shift is given by (3.2.5). At the horizon, (3.2.19) holds, so we have

$$\beta = \frac{\dot{f}}{2} + \frac{1}{2}. \tag{4.6.1}$$

From (3.2.9) we can see that when no matter is crossing the horizon, $\beta = .5$ so the outgoing characteristic speed is zero. However, if $\dot{f} = 1$, then $\beta = 1$ and the outgoing characteristic speed is -1. In this case, the light cone is degenerate. In fact, from (3.2.5) we can see that if $\dot{f} = 1$, then $\beta = 1$ *everywhere.* Does $\dot{f}$ ever equal one? The most likely place for this to happen is the critical solution because that is when the "maximum" amount of energy is crossing the horizon for a given pulse shape. The values of β at the horizon and at the outer boundary ($r = 42\,M$) are plotted in Figure 4.19. This is for the critical solution with $\sigma = 2$, $d = 2$, and $c = 10$. β gets up around .95, but never reaches 1. The critical solution for pulses with $d = 4$ gives a slightly higher maximum β, but still less than one. I think it is likely that a narrow enough pulse could cause $\dot{f}$ to reach one for an instant, but this has not been verified.

Whenever $\beta > .5$, the outgoing characteristic speed is negative. Thus, outgoing pulses will appear to move inward. Figure 4.20 shows an evolution of $\frac{dM}{dr}$ for the critical solution referred to above. The frames are spaced $1\,M$ apart in time. The vertical scale changes at $t = 5\,M$ so the outgoing pulse can be observed. The vertical lines passing through the frames are to provide a common horizontal reference so the retrograde motion of the outgoing pulse

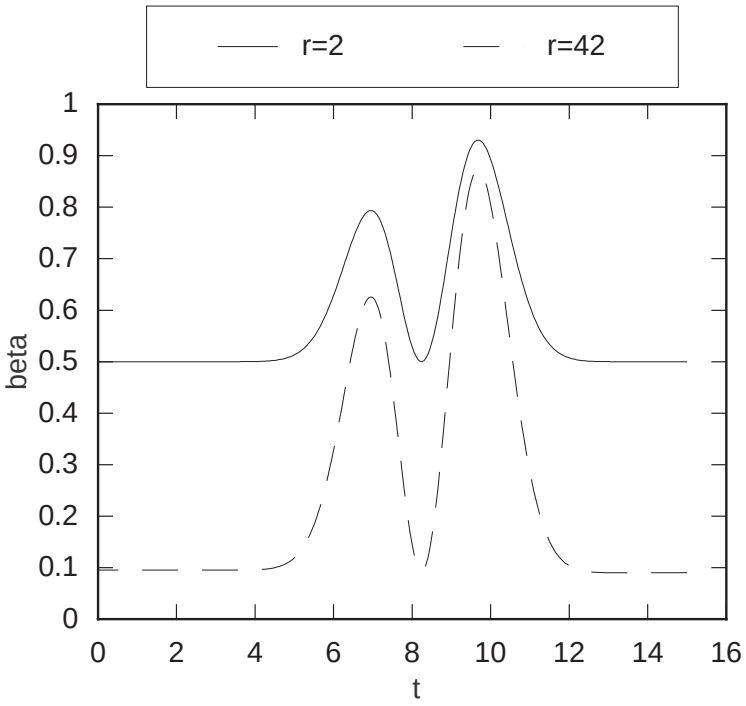

Figure 4.19. β at the horizon and the outer boundary for the critical solution with $\sigma = 2$, $d = 2$, and $c = 10$.

can be seen. There are two periods of backwards motion; one at about $7M$ and the other at about $10M$. These are the times when each of the "bumps" crosses the horizon. The retrograde motion is easier to see in Figure 4.21. This figure shows contours on an r verses t plot for the same evolution. Figure 4.22 shows a fairly weak field evolution of $\frac{dM}{dr}$ for comparison. There is no retrograde motion in this case.

4.7. Nonlinear Effects

There is a sharp "bump" at the front of the outgoing pulse in Figure 4.20. This feature is absent from the weak-field evolution of Figure 4.22 and is certainly amplitude dependent. Figure 4.23 shows a series of initial pulse shapes for data with various amplitudes and $\sigma = 2$, $d = 2$, and $c = 10$. Figure 4.24 shows the corresponding pulse shapes after scattering. The